AGU PUBLICATIONS

JGR

Journal of Geophysical Research: Oceans

RESEARCH ARTICLE

10.1002/2016JC011919

Wind relaxation and a coastal buoyant plume north of Pt. Conception, CA: Observations, simulations, and scalings

Sutara H. Suanda[1], Nirnimesh Kumar[2], Arthur J. Miller[1], Emanuele Di Lorenzo[3], Kevin Haas[4], Donghua Cai[4], Christopher A. Edwards[5], Libe Washburn[6], Melanie R. Fewings[7], Rachel Torres[8], and Falk Feddersen[1]

[1]Scripps Institution of Oceanography, University of California, San Diego, La Jolla, California, USA, [2]Civil and Environmental Engineering, University of Washington, Seattle, Washington, USA, [3]School of Earth and Atmospheric Sciences, Georgia Institute of Technology, Atlanta, Georgia, USA, [4]School of Civil and Environmental Engineering, Georgia Institute of Technology, Atlanta, Georgia, USA, [5]Ocean Sciences Department, University of California, Santa Cruz, California, USA, [6]Marine Science Institute, University of California, Santa Barbara, California, USA, [7]Department of Marine Sciences, University of Connecticut, Avery Point, Connecticut, USA, [8]Department of Physics and Engineering, North Park University, Chicago, Illinois, USA

Abstract In upwelling regions, wind relaxations lead to poleward propagating warm water plumes that are important to coastal ecosystems. The coastal ocean response to wind relaxation around Pt. Conception, CA is simulated with a Regional Ocean Model (ROMS) forced by realistic surface and lateral boundary conditions including tidal processes. The model reproduces well the statistics of observed subtidal water column temperature and velocity at both outer and inner-shelf mooring locations throughout the study. A poleward-propagating plume of Southern California Bight water that increases shelf water temperatures by $\approx 5°C$ is also reproduced. Modeled plume propagation speed, spatial scales, and flow structure are consistent with a theoretical scaling for coastal buoyant plumes with both surface-trapped and slope-controlled dynamics. Plume momentum balances are distinct between the offshore (>30 m depth) region where the plume is surface-trapped, and onshore of the 30 m isobath (within 5 km from shore) where the plume water mass extends to the bottom and is slope controlled. In the onshore region, bottom stress is important in the alongshore momentum equation and generates vertical vorticity that is an order of magnitude larger than the vorticity in the plume core. Numerical experiments without tidal forcing show that modeled surface temperatures are biased 0.5°C high, potentially affecting plume propagation distance and persistence.

Key Points:
- A multinested model reproduces the temperature and current variability at outer and inner-shelf sites around Pt. Conception
- Consistent with observations, the modeled response to wind relaxation is a poleward-propagating, coastally trapped, buoyant plume
- The model resolves well the differences between offshore and onshore plume dynamics

Correspondence to:
S. H. Suanda,
ssuanda@ucsd.edu

Citation:
Suanda, S. H. et al. (2016), Wind relaxation and a coastal buoyant plume north of Pt. Conception, CA: Observations, simulations, and scalings, *J. Geophys. Res. Oceans*, *121*, 7455–7475, doi:10.1002/2016JC011919.

Received 26 APR 2016
Accepted 14 SEP 2016
Accepted article online 20 SEP 2016
Published online 13 OCT 2016

1. Introduction

Point Conception, California marks an abrupt change in coastline orientation separating the Southern California Bight (SCB) and the Santa Maria Basin (SMB) (Figure 1). Many observational studies have captured the seasonal and interannual regional-scale ocean dynamics due to this topographic variability and wind-driven processes in the area [e.g., *Brink and Muench*, 1986; *Harms and Winant*, 1998; *Auad et al.*, 1999; *Winant et al.*, 2003; *Hickey et al.*, 2003; *Dever*, 2004; *Cudaback et al.*, 2005; *Fewings et al.*, 2015]. Between June and August, the mean wind direction is equatorward (upwelling-favorable), with maximum wind speed at the western edge of Pt. Conception rapidly decreasing in strength toward the center of the Santa Barbara Channel [*Dorman and Winant*, 2000]. During this period, the SMB continental shelf typically has recently upwelled cold surface water, adjacent to warmer waters within the SCB (Figure 1). These two disparate water masses mix in the Santa Barbara Channel (SBC) [*Hendershott and Winant*, 1996].

Event-scale (3–5 day) relaxations of the mean wind frequently occur in summer [*Dorman and Winant*, 2000]. The ocean response to these events is characterized by the poleward propagation of SBC water over the SMB shelf [e.g., *Melton et al.*, 2009; *Washburn et al.*, 2011]. Transport mechanisms are important as connectivity pathways across Pt. Conception for marine species such as giant kelp [*Johansson et al.*, 2015]. Because relaxation events are episodic, observational studies have relied on moorings or snapshots of surface scales from satellite sea surface temperature and HF radar currents when available [*Cudaback et al.*, 2005; *Melton et al.*, 2009; *Washburn et al.*, 2011]. Although differences in mean circulation have been identified between the outer (100 m water depth) and inner shelf (5–30 m water depth) [e.g., *Winant et al.*, 2003; *Cudaback*

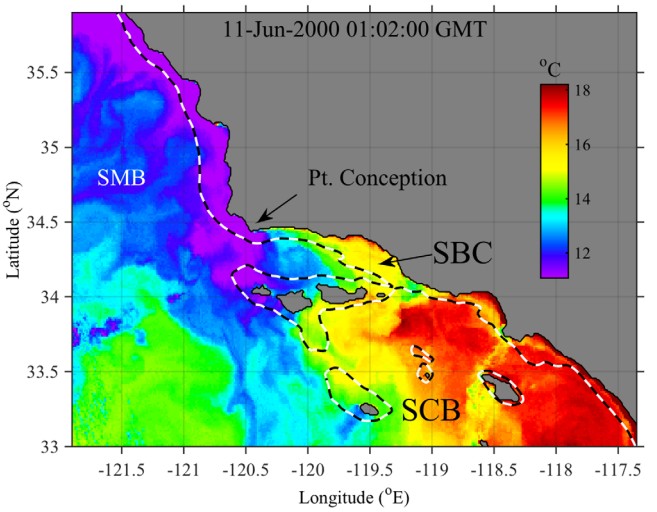

Figure 1. Sea surface temperature (SST) snapshot on 11 June 2000 observed by the Advanced Very High Resolution Radiometer (AVHRR). Regional locations are labeled; Santa Maria Basin (SMB), Southern California Bight (SCB), Santa Barbara Channel (SBC), and Pt. Conception. The dashed black-white contour is the 200 m isobath, approximately denoting the continental shelf.

et al., 2005], differences between the outer and inner shelf during event-scale wind relaxation are not well understood. Cross-shore vertical (*x*, *z*) sections and dynamical analysis during events are also lacking and difficult to observe without long-term *in situ* measurements with high spatial resolution. Here, we analyze the response to wind relaxation in a realistic coastal ocean numerical model, expanding prior observational results on thermally buoyant plumes in a geophysical setting.

Numerical models have been used to understand the regional-scale *O*(100 km) processes. For example, the large-scale seasonal spatial gradients in sea surface temperature (SST) [e.g., *Veneziani et al*., 2009], wind stress, and sea level pressure [e.g., *Wang*, 1997; *Oey et al*., 2004; *Dong and Oey*, 2005; *Hsu et al*., 2007] have been successfully reproduced and their dynamics elucidated by numerical models. In these studies, the horizontal grid resolution $\Delta x=5$ km is sufficient for regional scales but too coarse to explore shelf processes because the shelf is only $\approx$ 15 km wide. Additional modeling effort has focused on processes within the SCB [e.g., *Dong et al*., 2009], and recently include higher-frequency processes such as tidal-band processes through model nesting with horizontal resolutions of $\Delta x=250$ m [e.g., *Buijsman et al*., 2012; *Romero et al*., 2013] and up to $\Delta x=15$ m to resolve surfzone processes [*Kumar et al*., 2015].

Aspects of the coastal ocean response to wind relaxation, including the role of local topographic and bathymetric variability in creating along-shore pressure gradients have been described with numerical models [*Gan and Allen*, 2002a,2002b]. However, due to periodic boundary conditions, these studies did not include the effect of water masses originating beyond the simulated grid nor large-scale pressure gradient forcing [e.g., *Oke et al*., 2002; *Oey et al*., 2004; *Pringle and Dever*, 2009]. These considerations are particularly important around Pt. Conception, thus a multinested modeling approach is used here.

Previously compiled observations of many regional wind relaxation events show that the poleward-propagating ocean response on the SMB shelf is consistent with buoyant gravity current theory with the flow exiting SBC as the buoyancy source [*Washburn et al*., 2011]. Much of the theory for buoyant coastal current geometry and dynamics has emerged from scaling idealized laboratory and numerical experiments [e.g., *Yankovsky and Chapman*, 1997; *Lentz and Helfrich*, 2002; *Pimenta et al*., 2010]. These scalings provide estimates of propagation speed, geometry, and flow field characteristics as functions of coastal current transport, density contrasts ($\Delta\rho$), latitude, and bottom slope [*Lentz and Helfrich*, 2002]. The effects of realistic conditions such as temporally variable discharge and ambient coastal currents due to external forcings can also impact buoyant plume dynamics [e.g., *Yankovsky et al*., 2001; *Fong and Geyer*, 2002]. Observations and models have focused on salinity-driven coastal currents with relatively large $\Delta\rho$ between the current and ambient ocean waters. For example, $\Delta\rho$ from the Cheseapeake River current is 2–3 kg m^{-3} [*Lentz et al*., 2003]. Thermally buoyant coastal currents have a much smaller $\Delta\rho$ (e.g., $\Delta\rho=$ 0.1–0.9 kg m^{-3}), lack modeling attention on geophysical scales, and are less well-understood [*Woodson et al*., 2009; *Washburn et al*., 2011].

In this paper, a multinested nondata-assimilative model is configured for the SBC and SMB shelf and validated with available observations. The observations and numerical setup are described in section 2. Section 3 presents a general model-data time series and statistical comparison. Section 4 examines the observed and modeled kinematic response to a wind reversal event. In section 5, theoretical scalings used to interpret buoyant coastal currents are presented [*Lentz and Helfrich*, 2002], followed by methods used to characterize

the modeled current, and a comparison between the model, observations, and theory. The modeled coastal current is then used to provide a first approximation of the three-dimensional, time-varying structure of the SBC coastal current to expand on observational results (section 6). These include the evolving spatial scales, a contrast between offshore and onshore dynamics near the nose of the coastal current, and the effects of tidal mixing on its structure. Results are summarized in section 7.

2. Methods

2.1. Observations

Moored observations and model results are reported in a local coordinate system where x is the cross-shore, onshore positive, with the coast located at $x = 0$. The y coordinate is in the along-shelf direction, positive poleward. The mean sea surface is located at the vertical coordinate $z = 0$, positive upward with the ocean bottom at $z = -h$, where h is the local water depth. Modeled and observed currents are rotated into their principal axes as defined by the depth-averaged subtidal flow at each location. Once rotated, currents along the major axis are considered to be in the along-shelf (v) direction, while currents along the minor axes are oriented in the cross-shore (u) direction.

In situ temperature and velocity observations are from two observational programs whose mooring deployments overlapped with the study period (Summer, 2000). The focus here is on subtidal-frequencies, thus observations and modeled temperature and velocity are low-pass filtered (retaining periods > 33 h). Over the outer shelf (100–200 m water depth), four moorings deployed from the Santa Barbara Channel-Santa Maria Basin Coastal Circulation Study (1989–2005) measured temperature ($z = -1, -5, -25, -45, -65$, and -100 m) and currents with Vector Measuring Current Meters ($z = -5$ m) [*Harms and Winant*, 1998; *Winant et al.*, 2003] (Figure 2). In this work, the northernmost outer-shelf mooring is referred to as the Santa Maria Basin (SMB) mooring. Naming convention for locations at the western (SMIN, SMOF) and eastern (ANMI) entrances of the Santa Barbara Channel follows previous studies.

Inner-shelf (15 m water depth) temperature and velocity observations are from the Partnership for Interdisciplinary Studies of Coastal Oceans (PISCO) moorings (1998–present) [e.g., *Cudaback et al.*, 2005; *Melton*

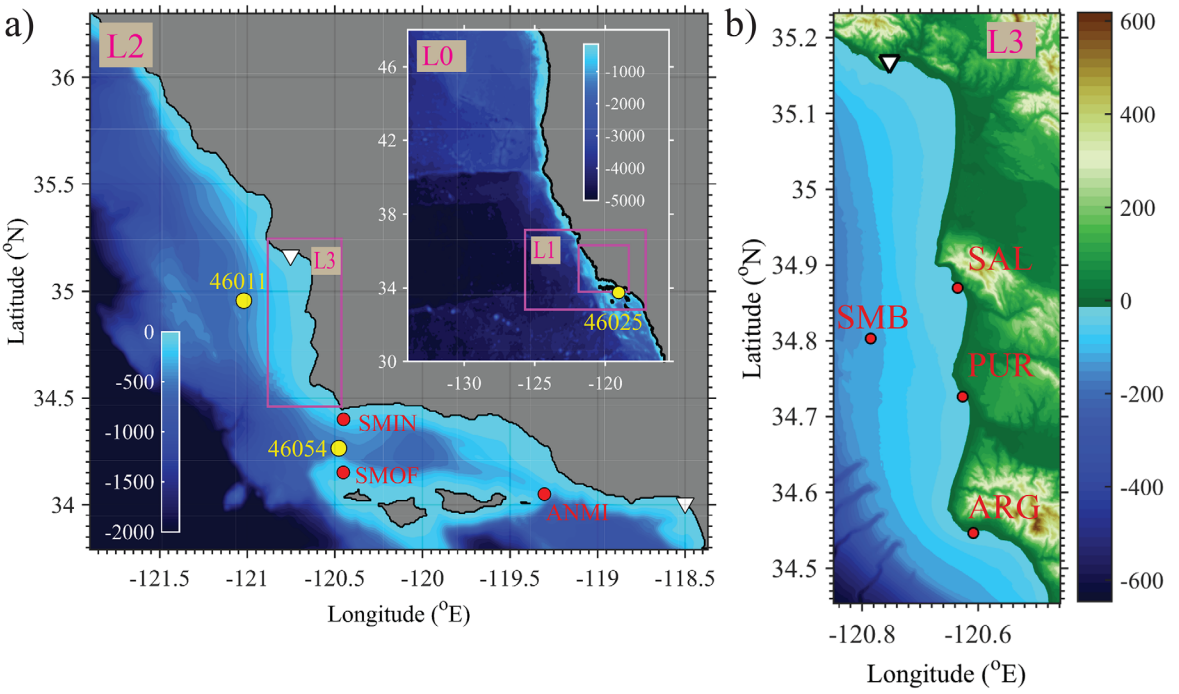

Figure 2. Four simulation grids and observation locations: (a) second level of nested grid (**L2**, see section 2.2 for grid dimensions and resolution). Yellow circles mark NDBC buoys used in this study, 46011, 46054, and 46025. Lower-level grids are shown in inset (**L0** and **L1**). Colorbar is the vertical coordinate z in meters. (b) **L3** grid. White triangles mark the Port San Luis (within L3) and Santa Monica tide gauges. In both plots, red circles are moored observation locations. Outer-shelf moorings are in 100 m depth (SMIN, SMOF, SMB), except for ANMI (200 m depth). From south to north, inner-shelf (15 m depth) moorings are Pt. Arguello (ARG), Pt. Purisma (PUR), and Pt. Sal (SAL).

et al., 2009; *Fewings et al*., 2015; *Aristizábal et al*., 2016]. Temperature observations were collected at three depths ($z=-4$, -10, and -15 m) from Pt. Arguello (ARG), Pt. Purisma (PUR), and Pt. Sal (SAL) mooring locations (Figure 2). Velocity measurements at PUR were available from an upward-looking RDI 600 kHz Acoustic Doppler Current Profiler (ADCP) with good data from $z=-3$ m to $z=-14$ m.

Supplementary observations include atmospheric variables of air pressure and winds from NDBC buoy 46011, 46054, 46025, and sea level from NOAA Port San Luis and Santa Monica tide gauges (Figure 2). Additionally, satellite observations of sea surface temperature (SST) from the Advanced Very High Resolution Radiometer (AVHRR) satellite are used to provide the regional oceanographic setting and qualitative comparison to modeled results (section 4.1).

2.2. Numerical Model

The model used is the Rutgers Regional Ocean Modeling System (ROMS), a three-dimensional, terrain-following, open source numerical model that solves the Reynolds-averaged Navier-Stokes equations with hydrostatic and Boussinesq approximations [*Shchepetkin and McWilliams*, 2005; *Haidvogel et al*., 2008; *Shchepetkin and McWilliams*, 2009; *Warner et al*., 2010]. The modeling system is configured to run a series of nested offline simulations whereby the largest relevant forcing scales are simulated on a coarse grid and variability is transmitted to smaller domains of higher horizontal resolution through open boundary conditions [e.g., *Wilkin*, 2006; *Penven et al*., 2006; *Springer et al*., 2009; *Dong et al*., 2009; *Ganju et al*., 2011; *Romero et al*., 2013; *Kumar et al*., 2015, 2016]. At subsequent levels of nesting, additional smaller-scale forcing mechanisms (i.e., tides) are then added.

Model bathymetry is from the NOAA NGDC database (1 arc second resolution—https://www.ngdc.noaa.gov/). Multiple nested grids are configured to simulate the SMB continental shelf (Figure 2). Both bathymetric and coastline resolution are increased at each level of nesting. The lowest level, the outermost grid (**L0**, $\Delta x=3$ km, 556×541 grid cells), extends from the Baja peninsula to Washington State spanning 18° of latitude and longitude encompassing the eastern Pacific basin. Subsequent higher level child grids have increased horizontal resolution (**L1**, $\Delta x=1$ km, 770×392 grid cells and **L2**, $\Delta x=600$ m, 546×386 grid cells) until a final grid which resolves inner-shelf processes (**L3**, $\Delta x=200$ m, 194×362 grid cells). Standard nesting techniques are used to ensure volume conservation and bathymetry at child grid boundaries match the parent grid [e.g., *Mason et al*., 2010].

The outermost simulation is run on **L0**, forced by daily averaged, realistic atmospheric fields (see 2.2.2 below) and climatological lateral boundary conditions from the World Ocean Atlas. The model is similar to that evaluated in *Veneziani et al*. [2009], with statistically reasonable mean and mesoscale varying California Current System, although with three times higher horizontal resolution in both zonal and meridional directions. The simulation has 42 vertical levels, and applies the Generic Length Scale (GLS) vertical mixing scheme with $k-\omega$ parameters to solve for vertical eddy viscosity and diffusivity [*Warner et al*., 2005]. Radiation boundary conditions are applied to barotropic fields to allow outgoing energy [*Chapman*, 1985; *Flather*, 1976; *Mason et al*., 2010], and both radiation and nudging are used for baroclinic boundary conditions [*Marchesiello et al*., 2001]. Model boundary values are nudged to incoming information with a 1 day time scale ($\Delta\tau=1$ day) and are weakly nudged to outgoing information ($\Delta\tau=365$ days). A roughly 130 km wide sponge layer with horizontal eddy viscosity, that increases from the interior value of 1 $m^2\,s^{-1}$ to a boundary value of 200 $m^2\,s^{-1}$, is placed along the open boundaries. Model spin-up is conducted for 6 years with climatological boundary conditions and climatological surface forcing, followed by a 1 year-long integration with surface forcing of realistic spatial and temporal variability (see section 2.2.2).

To downscale this **L0** simulation, sea level, tracer, and momentum fields are interpolated at each time step to the **L1** grid boundaries (boundary conditions) and are interpolated to **L1** interior grid points for the first time step of the nested simulation (initial conditions). The **L1** simulation starts on 1 May 2000, with baroclinic velocity and tracer values clamped at the boundaries and no sponge layer. Subsequently, simulations on the **L2** grid use results from **L1** and simulations on **L3** use results from **L2** as boundary conditions. The **L2** and **L3** simulations are integrated for a 60 day period covering June–July 2000. All nested grids share the same 42 vertical levels and sigma-coordinate parameter settings as the parent simulation. To accommodate the addition of tides (see 2.2.1), in **L2** and **L3** tracer and incoming baroclinic velocities are strongly nudged ($\Delta\tau=6$ h on **L2** and $\Delta\tau=1$ h on **L3**) and outgoing velocities are weakly nudged ($\Delta\tau=365$ days on all grids). Similar to *Kumar et al*. [2015] in **L2** and **L3** a horizontal eddy viscosity of 0.1 $m^2\,s^{-1}$ is applied to

Table 1. Observed and Modeled Tidal Constituents[a]

	Sea Level		Velocity	
Constituent	amp (m)	ph (°)	amp (m s^{-1})	ph (°)
S2	0.10 (0.12)	168.3 (164.4)	0.007 (0.009)	179.7 (178.9)
M2	0.49 (0.47)	170.7 (167.6)	0.033 (0.039)	103.4 (117.4)
O1	0.21 (0.19)	186.2 (189.8)	0.008 (0.003)	115.5 (49.7)
K1	0.42 (0.43)	226.1 (221.5)	0.007 (0.008)	240.8 (25.8)

[a]Comparison of observed to modeled (in parentheses) major tidal constituents for sea level and major-axis velocity at PUR (15 m water depth). Amplitude (amp) and phase (ph) are reported from harmonic analysis with ph = 0° marking the beginning of the time series.

dampen small-scale numerical instabilities without altering relevant modeled dynamics. Additional simulations on higher nests with grids capable of resolving surface gravity wave forcing were also conducted and will be described in future manuscripts.

2.2.1. Tides

Tidal forcing is not included in the outermost **L0** or first nested **L1** simulation. Harmonic sea level and barotropic velocities from eight astronomical tidal constituents (K_2, S_2, M_2, N_2, K_1, P_1, O_1, Q_1) and two overtides (M_6, M_4) are applied as boundary forcing on the **L2** simulations from the ADCIRC tidal model [*Mark et al*., 2004]. Within the **L2** simulation, the interaction of tidal forcing, variable bottom topography, and stratification can produce internal waves of tidal periodicity (internal tides) which propagate throughout the numerical domain and are transmitted to the higher-resolution domain **L3** via the lateral boundary conditions as described above.

Barotropic tides are validated by comparison to observations of sea level from the Port San Luis tide gauge and depth-averaged velocity from PUR (Table 1). Harmonic analysis conducted with the T_TIDE package [*Pawlowicz et al*., 2002] shows that the four largest-amplitude tidal constituents of sea level and major-axis velocity compare well (section 3 and Table 1). The phases of the diurnal velocity constituents and the amplitude of O_1 velocity are poorly modeled, potentially due to diurnal sea breeze effects not included in the model.

2.2.2. Model Surface Forcing

The Coupled Ocean-Atmosphere Mesoscale Prediction System (COAMPS) model was run in a quadruply nested configuration over the northeast Pacific and western North America domain [*Hodur et al*., 2002; *Doyle et al*., 2009]. Output from the four grids is daily averaged and combined to produce a ROMS forcing file on **L0**. The resolution of the atmospheric forcing in the SMB–Pt. Conception region is 9 km, which is interpolated to higher horizontal resolution for all ROMS child grid simulations. Although previous regional studies suggest the importance of wind forcing with resolution higher than 9 km [e.g., *Oey et al*., 2004; *Dong and Oey*, 2005], the COAMPS resolution produces good model-data agreement for bulk temperature and current dynamics over the entire SBC–SMB shelf region during the period of study, albeit with some differences in the lee of small coastal headlands (section 3).

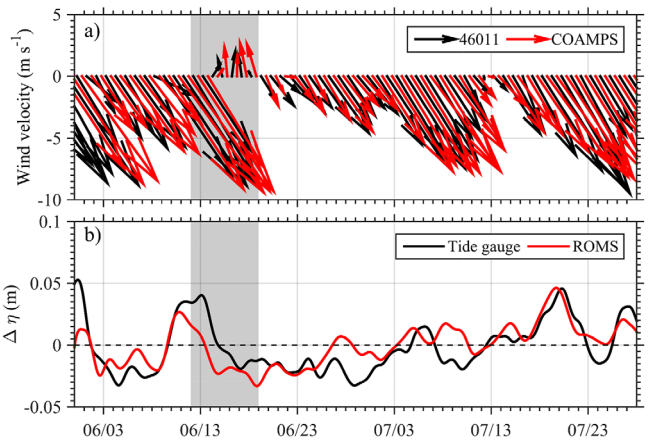

Figure 3. Time series of observed (black) and modeled (red) (a) daily-averaged vector winds from NDBC buoy 46011 and COAMPS modeled (vectors are offset 0.5 day for clarity), and (b) Santa Monica to Port San Luis subtidal sea level differences $\Delta\eta$. NDBC buoys and tide gauge locations are noted with yellow circles and white triangles, respectively, in Figure 2a. The period of propagating poleward flow analyzed in section 4 is shaded.

The direction, amplitude, and temporal variability of the COAMPS wind compares well ($r^2 > 0.87$) to the observed wind at NDBC buoy 46011 during the simulation period (Figure 3a). Observed (modeled) principal axis winds oriented 54° (52°) counterclockwise from north are used in section 3 for correlation to observed and modeled ocean fields. Spatially variable COAMPS winds are similarly well correlated to the other NDBC buoys in the region (not shown). Consistent with typical summer conditions in the area [e.g., *Dorman and Winant*, 2000; *Winant et al*., 2003; *Melton et al*., 2009], winds were predominantly upwelling-favorable with an extended wind reversal between 13 June and 20 June and a wind relaxation around 13 July.

2.2.3. Large-Scale Sea Level Variations

In both models and observations, regional sea level variations induce along-shelf pressure gradient forces that control poleward flows over the continental shelf from seasonal [e.g., *Harms and Winant*, 1998; *Fewings et al.*, 2015; *Connolly et al.*, 2014] to subtidal [e.g., *Brink and Muench*, 1986] time scales. Along-shelf sea level, variations are generated over scales ranging from the entire (1000 km) North American west coast [e.g., *McCreary*, 1981] to regional (10–100 km) coastline variability [e.g., *Gan and Allen*, 2002a; *Oey et al.*, 2004]. For example, over 2000 km of the North American west coast, seasonal sea level differences $\Delta\eta \approx 0.10$ m were well reproduced in a year-long 9 km resolution model nested within a global model [*Connolly et al.*, 2014]. On smaller spatial and time scales, a nested simulation of the northern California shelf produced sea level differences $\Delta\eta \approx 0.03$ m over 150 km at 20 day time scale [*Pringle and Dever*, 2009], although not compared to observations. Accurate model simulation of sea-level differences at subtidal time scales and a range of spatial scales requires both large-scale and local dynamics to be resolved.

Here, the ability of the multinested shelf model to reproduce observed larger-scale sea level differences $\Delta\eta$ is tested from the Santa Monica and Port San Luis tide gauges, separated by an along-shelf distance of $\approx$ 300 km (white triangles in Figure 2). Model sea level differences $\Delta\eta$ are estimated at modeled grid points corresponding to tide gauge locations (Figure 3b) where Santa Monica is within **L2** and Port San Luis is within **L3**. Observed and modeled $\Delta\eta$ are generated by first removing the time-mean (over the 60 day simulation) sea-level at each tide gauge. Harmonic analysis with T_TIDE [*Pawlowicz et al.*, 2002] accounted for $\approx$ 98% of the sea-level variance and was removed. Any residual tidal-band variability was additionally removed by a low-pass filter (33 h filter cut-off). Finally, $\Delta\eta$ is calculated as the difference of the Port San Luis time series subtracted from Santa Monica. As the inverse barometer effect is not dynamically included in the ROMS model, these effects are removed from observed $\Delta\eta$ by subtracting atmospheric pressure measured at NDBC 46011 (46025) from the Port San Luis (Santa Monica) tide gauge sea level record [*Melton et al.*, 2009]. The observed and modeled $\Delta\eta$ compare well (Figure 3b), are correlated ($r^2 = 0.48$) with similar variability ranging from 0.05 to -0.03 m and a mean model $\Delta\eta$ bias of less than 10^{-4} m. This demonstrates that the multinested approach accurately generates sea-level differences over the larger SCB scale of 300 km. However, these $\Delta\eta$ should not specifically be interpreted as local pressure gradients surrounding individual headlands such as Pt. Conception (with $\approx$10 km length scales).

3. Model-Data Comparisons

For model-data comparison, modeled **L3** temperature and velocity are extracted from the location of the outer (SMB) and inner-shelf (ARG, PUR, SAL) moorings. Modeled **L2** results are extracted at SMIN, SMOF, and ANMI moorings located outside the **L3** domain. Unless otherwise stated, all correlations reported are significant at 95% confidence.

Observed and modeled temperature time series are compared and discussed in relation to NDBC 46011 daily averaged principal axis wind forcing, oriented to the south-east and considered representative of the regional wind forcing [e.g., *Melton et al.*, 2009]. Although the moorings at the western SBC entrance are closer to NDBC 46054, wind to surface temperature correlations are not improved by using these winds during the spring-summer [*Harms and Winant*, 1998]. At the outer-shelf SMB mooring, modeled and observed near surface temperature time series are in good agreement and are correlated ($r^2 > 0.3$) to the principal axis wind (Figure 4a). The most pronounced warming signal in both model and observations is a near-surface $\approx$5°C temperature increase during a reversal of the predominantly northwesterly wind (12 June to 19 June). Modeled temperature is biased high $\approx$2°C due to a coastal summer-time bias in the COAMPS heat flux applied to all model nests [*Veneziani et al.*, 2009]. At the midwater column of the outer-shelf moorings ($z = -65$ m), neither observed nor modeled temperature is strongly correlated to the principal axis wind, indicative of other forcing mechanisms of temperature at depth at these locations (Figures 4a and 4c). Both outer and inner-shelf sites show a distinct sense of northward propagation to the warming signal as the arrival at southern moorings (SMIN, ARG) lead the northern sites (SMB, SAL) [*Melton et al.*, 2009; *Washburn et al.*, 2011]. In contrast to the outer-shelf moorings, water temperatures at all depths at all 3 inner-shelf moorings are correlated to the wind ($r^2 > 0.5$) and experience the marked warming during wind reversal (Figures 4b and 4d).

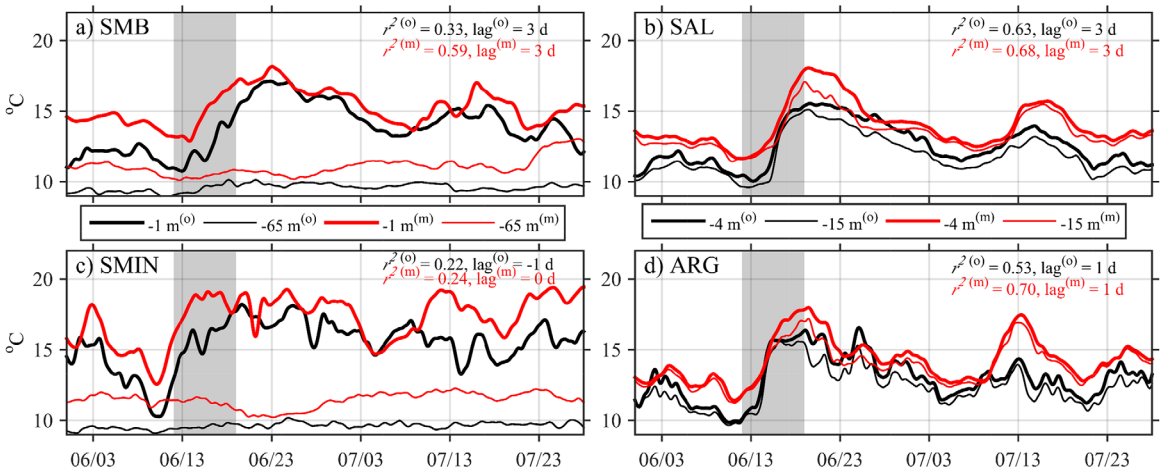

Figure 4. Model-data comparison of low-pass filtered temperature at (a) SMB, (b) SAL, (c) SMIN, and (d) ARG moorings. Observations (black) and model (red) results are shown at the surface-most (thick lines, $z = -1$ m in Figures 4a and 4c, $z = -4$ m in Figures 4b and 4d), midwater column (thin lines, $z = -65$ m in Figures 4a and 4c) and near-bottom (thin lines, $z = -15$ m in Figures 4b and 4d) measurement locations. Squared correlation coefficients (r^2) and the lag which maximizes the correlation between near surface temperature to principal axis winds are noted in each plot. The period of propagating poleward flow analyzed in section 4 is shaded.

Observed major-axis (along-shelf) currents are well-reproduced by the model at both the outer-shelf SMB and inner-shelf PUR moorings (Figure 5a). Modeled flow is stronger than observations and more strongly correlated to the principal axis wind ($r^2 > 0.6$ in model, $r^2 > 0.3$ in observations). The largest poleward flow signals (>0.2 m s^{-1}) are seen around 06/14 in both observations and the modeled flow (Figure 5a). Although near-bottom along-shelf flows are mostly weak on the inner shelf (<0.005 m s^{-1}), they can be directed poleward throughout the water column during wind reversal events (Figure 5b and *Washburn et al.* [2011]).

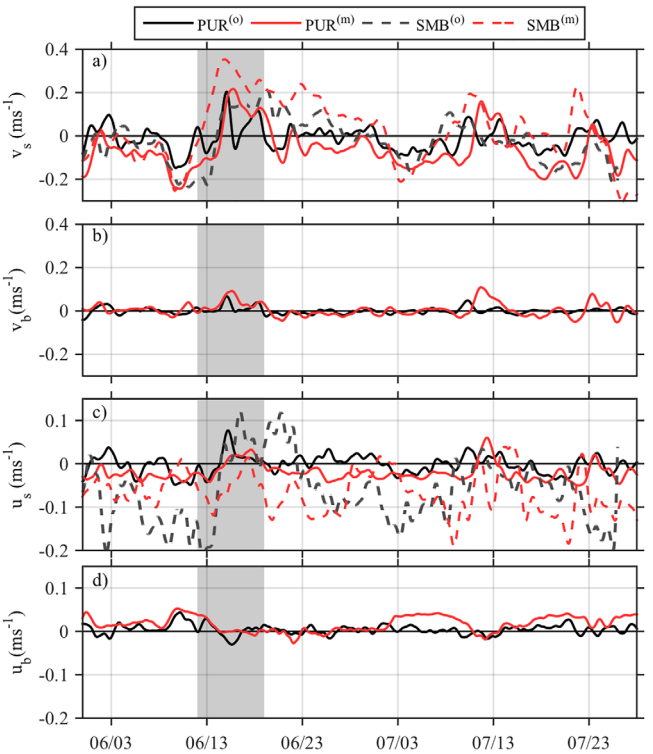

Figure 5. Model-data comparison of low-pass filtered velocity at SMB and PUR moorings. Velocities are oriented in the direction of their principal axes such that along-shelf poleward is $+v$ and cross-shelf shoreward is $+u$. (a) Near surface along-shelf velocity v_s. (b) Near bottom along-shelf velocity v_b. (c) Near surface cross-shelf velocity u_s. (b) Near bottom cross-shelf velocity u_b. Period of propagating poleward flow analyzed in section 4 is shaded.

In the cross-shore direction, near-surface SMB currents are highly variable and only weakly correlated to the principal axis winds (Figure 5c, dashed). The near-surface flow on the inner shelf is directed offshore over most of the study period and is opposite at the near-bottom, consistent with the wind forcing with correlations $r^2 > 0.4$ in both model and observations (Figure 5c, solid). Near-surface cross-shore flows are onshore in the surface during the relaxation period. Observed correlations between the flow in this location and the wind are consistent with previously reported values [*Fewings et al.*, 2015].

3.1. Vertical Structure of Mean and Subtidal Standard Deviations

At both outer and inner-shelf locations, the modeled and observed time-mean temperatures are similar

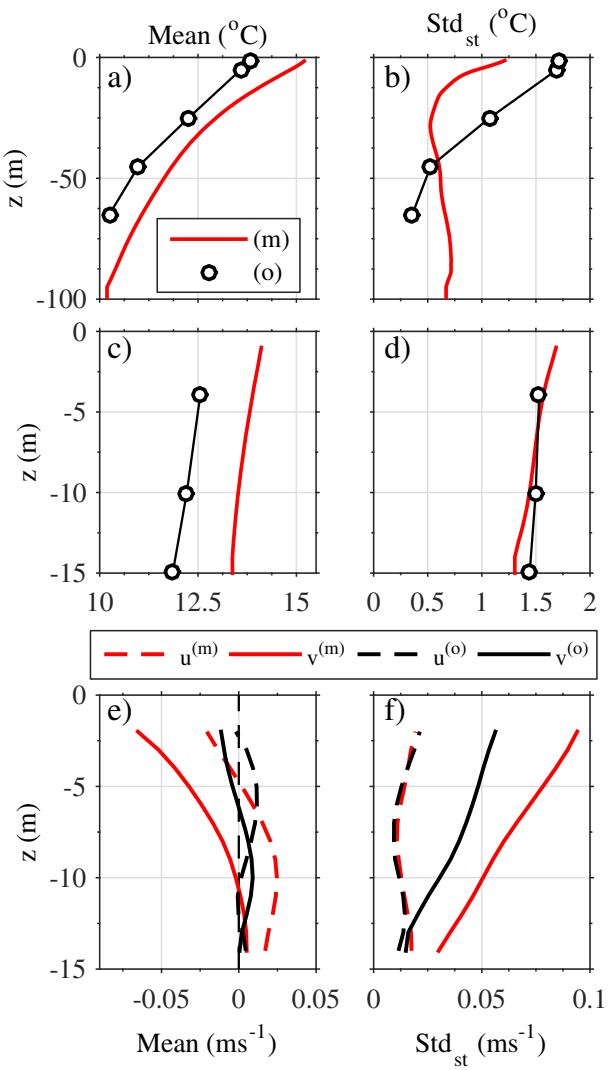

Figure 6. Observed (black) and modeled (red) profiles of subtidal temperature and velocity statistics. Time mean (left column) and standard deviation (right column) of temperature at (a, b) SMB and (c, d) PUR, and velocity at (e, f) PUR. Velocities are in the direction of the major principal axis, *v* (solid lines) and the minor axis, *u* (dashed).

except that model temperatures are biased ≈1.5°C high (Figures 6a and 6c). Both the observed and modeled mean vertical temperature gradient is about 0.06°C m^{-1}. At SMB, low-frequency standard deviations are surface intensified, although modeled values are 0.5°C smaller (Figure 6b). Subtidal temperature standard deviations compare well at PUR (Figure 6d) with a magnitude of 1.5°C. Comparisons at other mooring locations yield similar results (not shown), a summary of model-data temperature error statistics are given in Appendix A.

Modeled and observed velocity profile statistics at PUR are mostly comparable, with some differences in magnitude and structure (Figures 6e and 6f). In the direction of the major axis (along-shore, *v*), both observed and modeled mean flows are surface intensified and equatorward (<0) in the near-surface, although the modeled mean is ≈ 0.05 m s^{-1} stronger (Figure 6e). The observed mean flow is weakly (≈ 0.01 m s^{-1}) poleward at depths below $z = -6$ m, whereas the weak modeled mean poleward flow is below $z = -12$ m. In the minor axis direction (cross-shore, *u*), the observed positive onshore flow is higher in the water column than in the modeled profile. In general, at PUR the mean flow in both observations [*Fewings et al.*, 2015] and the model are weak compared to the subtidal standard deviations (Figure 6f). Both modeled and observed major-axis variability is much larger than the minor axis, though modeled variability is ≈ 0.03 m s^{-1} larger than observed throughout the water column. Observed and modeled differences in low-frequency dynamics are possibly due to unresolved processes in the lee of PUR. Specifically, the 200 m horizontal resolution bathymetry could be too smooth. Additionally, although the COAMPS wind field compares well to observed offshore NDBC buoy observations, spatial variability in the lee of coastal headlands is underresolved [*Dong and Oey*, 2005; *Hsu et al.*, 2007]. Finally, prior results from the inner-shelf in this location show barotropic along-shore pressure gradients to dominate over baroclinic pressure gradients [*Fewings et al.*, 2015]. Without a dense mooring array, horizontal density differences which drive baroclinic pressure gradient forces cannot be estimated. Further observations are needed to determine their importance.

4. Evolving Response to Wind Relaxation

4.1. Regional Scale: Satellite-Model Comparison

After an increase in the strength of upwelling-favorable winds between 9 June and 11 June, winds begin to relax and reverse direction between the 14 and 18 June (Figure 3a). On regional scales, the modeled response to changing wind patterns is qualitatively similar to available satellite SST observations (Figure 7).

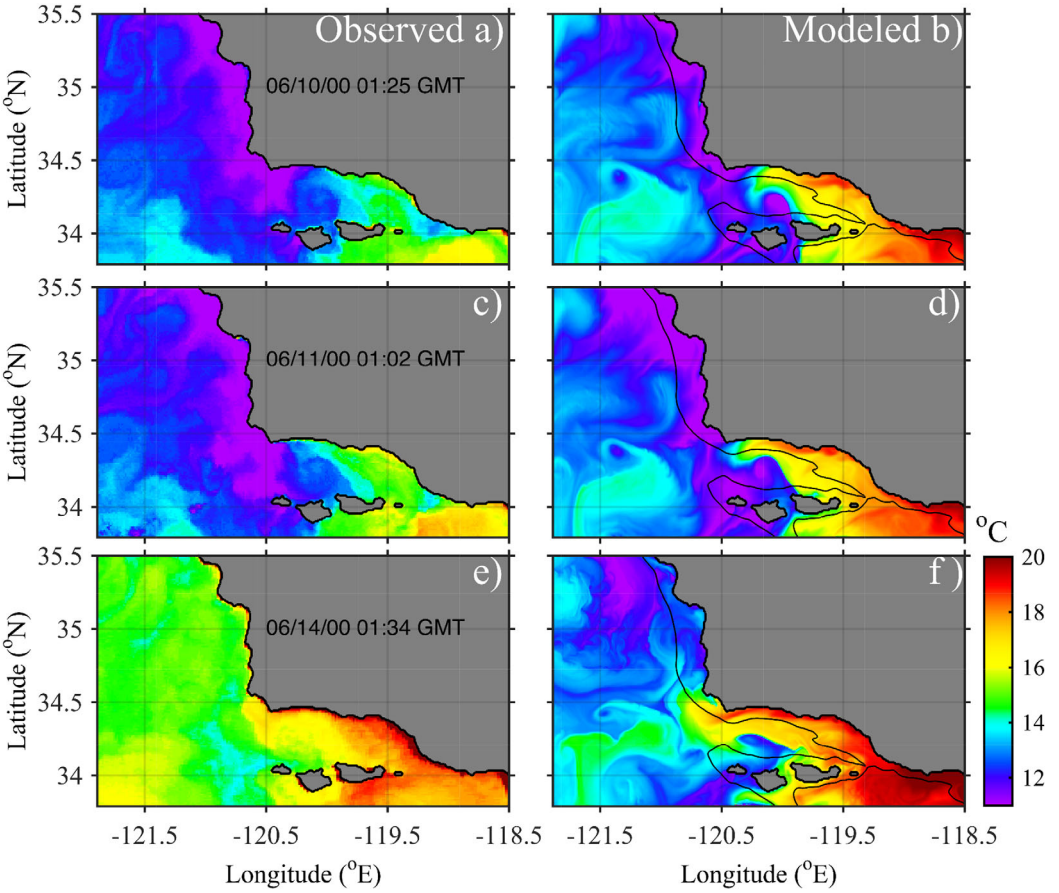

Figure 7. Regional SST snapshots around wind reversal period. SST observed by AVHRR (a, c, e) and corresponding modeled SST (b, d, f) from nearest hour to observations. In the satellite imagery, there has been no attempt at either cloud contamination masking nor temperature calibration. Portions of Figures 7c and 7e were shown in *Melton et al.* [2009]. Mean bias (1.5°C) has been removed from modeled results.

Consistent with the in situ model bias (section 3), 1.5°C is subtracted from all modeled SST panels to facilitate the comparison (Figures 7b, 7d, and 7f). Prior to the wind relaxation, warm water (>14°C) is found to the east of Pt. Conception with a well-developed cyclonic eddy in the center of the Santa Barbara Channel in both observations and the model (Figures 7a and 7b). As winds briefly increase (11 June), warm SBC water advances toward Pt. Conception and the coastal upwelling signature remains over the SMB shelf (Figures 7c and 7d). Entering the reversal period (14 June), SBC water rounds Pt. Conception and appears to split into two branches: a portion that flows poleward onto the SMB shelf (discussed below) and one that spreads southward toward San Miguel Island potentially recirculating back into SBC. Further satellite imagery of the event was not available due to cloud contamination.

4.2. SMB Shelf Scale

During wind reversal, the observed [*Washburn et al.*, 2011] and modeled coastal ocean response is the poleward-propagating flow of warm water as seen in modeled sea surface temperature (SST) and cross-shore temperature transect snapshots (Figure 8). Preceding the reversal (13 June), modeled SST patterns are typical of upwelling conditions on the SMB shelf including colder water in the lee of headlands, and smaller-scale filaments stretching seaward from the coastline (Figures 8a and 8d). One day later (14 June), warmer water (≈14°C) has begun to fill the near-surface of the SMB shelf potentially due to a combination of increased surface heating and the return of offshore waters in response to relaxing winds (Figure 8b). An even warmer water mass (>16°C) can be seen to the south of ARG, not yet reaching the PUR $x - z$ transect (Figure 8e). Two days later, the front has passed PUR, 17°C water extends across the entire shelf and warm water also fills the upper 20 m of the water column (Figures 8c and 8f). The leading edge of the warm water is located offshore of the coastline, forming a nose which appears detached from the coast.

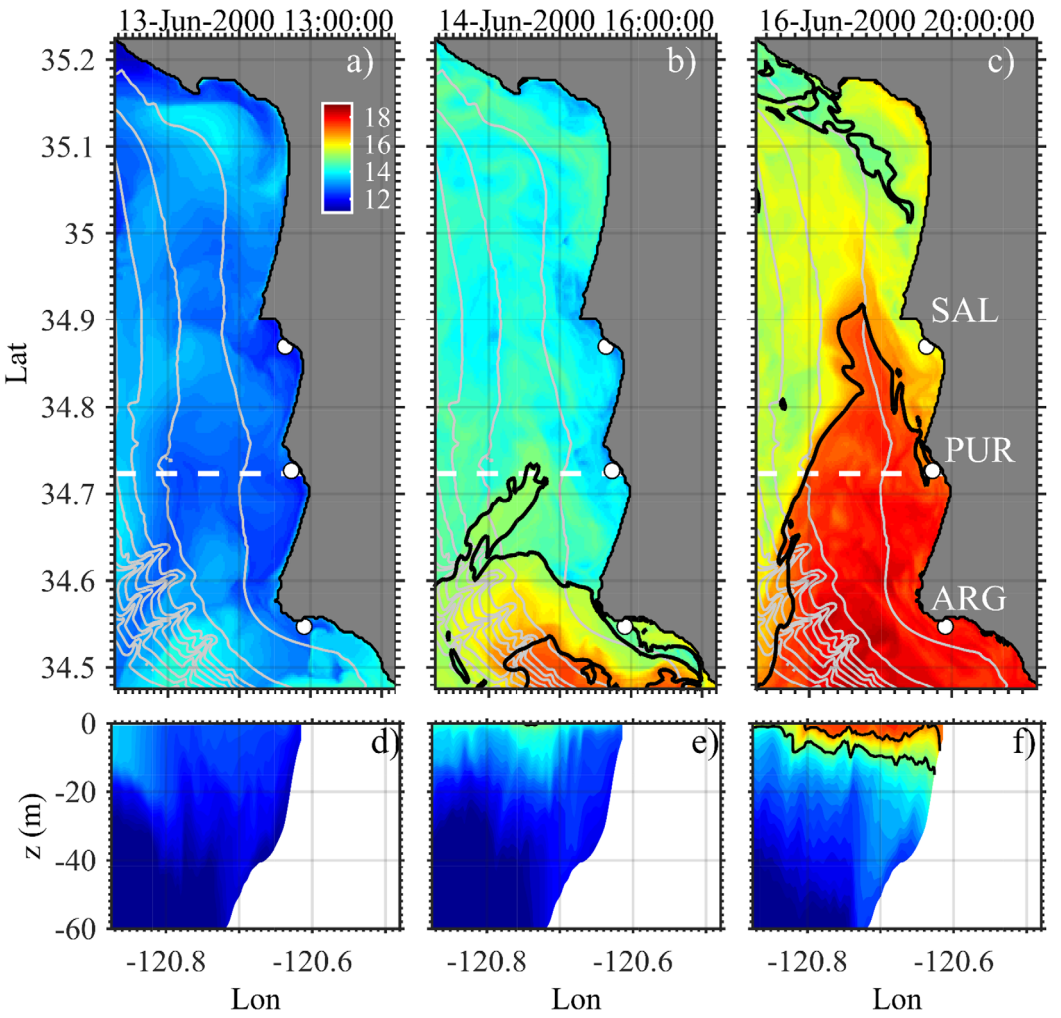

Figure 8. Three snapshots of modeled (a–c) SST and (d–f) cross-shore and vertical temperature transects at latitude of Pt. Purisma mooring (34.73°N, white dashed line in Figures 8a–8c). Bathymetry contours are in 50 m intervals, and the 15°C and 17°C isotherms are contoured black.

5. A Coastally Trapped Buoyant Plume

5.1. Theory

An idealized buoyant coastal current attached to a sloping shelf in a fixed reference frame [*Lentz and Helfrich*, 2002; *Washburn et al.*, 2011] is illustrated in Figure 9. Away from the source and bounded by a coast, a buoyant plume of fluid with density ρ discharging into a rotating fluid of higher density $\rho+\Delta\rho$ takes the limiting form of either a surface-trapped or a bottom-slope controlled coastal current [*Yankovsky and Chapman*, 1997]. In the vertical wall limit (located at $x = 0$), the front (nose) of a purely surface-trapped plume propagates in the direction of a Kelvin wave ($y > 0$) at the internal wave speed,

$$c_w = (g' h_p)^{1/2}. \tag{1}$$

Here, g' is the plume reduced gravity $g\Delta\rho/\rho$ and h_p is the depth where the plume intersects the sloping shelf (Figure 9). This occurs at an offshore location $x = x_p$, termed the "foot" of the plume. Combining volume conservation with the assumption that the equilibrium along-shelf frontal velocity is geostrophically balanced, *Yankovsky and Chapman* [1997] derive an expression for h_p,

$$h_p = \left(\frac{2Qf}{g'}\right)^{1/2}. \tag{2}$$

The additional parameters are the Coriolis frequency f and the plume volume transport $Q\,(\mathrm{m^3\,s^{-1}})$.

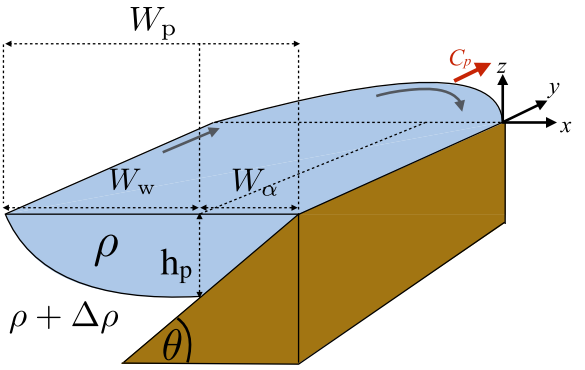

Figure 9. Schematic of idealized buoyant coastal current attached to a shelf with slope θ in a fixed reference frame [*Lentz and Helfrich*, 2002; *Washburn et al.*, 2011]. The coastal current has density ρ, separated from ambient ocean water of density $\rho+\Delta\rho$. The portion of the current attached to the slope has width W_α, at water depth h_p. The offshore (surface-trapped) portion of the current has width W_w, and the total plume width is $W_p = W_w + W_\alpha$. Currents are denoted by gray arrows, including a geostrophic along-shelf flow near the offshore edge, and an onshore flow at the leading edge of the coastal current. The leading edge propagates at speed c_p (red arrow) oriented towards the $+y$ direction.

A bottom-slope controlled plume propagates at a speed

$$c_\alpha = \theta g'/f, \tag{3}$$

similar to a topographic wave where θ is the bottom slope [*Lentz and Helfrich*, 2002]. These results are generalized to give the propagation speed of intermediate plumes,

$$c_p \propto \frac{c_w}{1+c_w/c_\alpha}. \tag{4}$$

The ratio c_w/c_α determines whether plumes are governed by primarily surface-trapped ($c_w/c_\alpha \ll 1$) or slope-controlled ($c_w/c_\alpha \gg 1$) dynamics [*Lentz and Helfrich*, 2002].

Thermally buoyant plumes such as the relaxation flows at Pt. Conception are in an intermediate parameter regime ($c_w/c_\alpha \approx 1$) [*Washburn et al.*, 2011] because density differences with the ambient fluid are much smaller than in river plumes. The generalized intermediate plume has an offshore region that is surface-trapped, and an onshore region that is slope-controlled. Scalings for the width of these plume regions, the surface-trapped portion $W_w \propto c_w/f$, and slope-attached portion $W_\alpha \propto h_p/\theta$, are combined to provide a scale relation for the width of the entire plume $W_p = W_w + W_\alpha$ [*Lentz and Helfrich*, 2002],

$$W_p \propto \frac{c_w}{f}(1+c_w/c_\alpha). \tag{5}$$

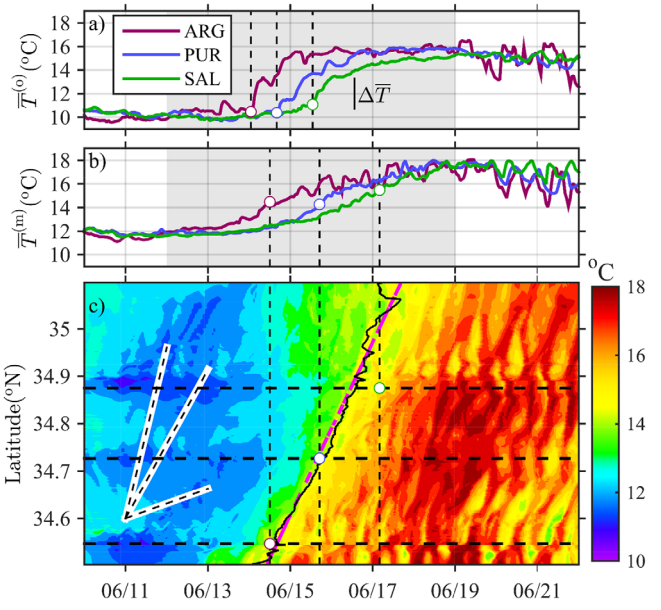

Figure 10. (a) Observed $\overline{T}^{(o)}$ and (b) modeled $\overline{T}^{(m)}$ depth-averaged temperature from three inner-shelf mooring locations spanning ≈ 35 km. Vertical-dashed lines mark the warm front arrival as determined by *Washburn et al.* [2011] methods (see 5.2.1), applied separately to model and observations. (c) Modeled time-latitude contour plot of depth averaged temperature following the 15 m isobath. Locations of headland moorings are noted by horizontal dashed lines. The 14.5 degree isotherm is noted (black contour), with a linear regression between latitude and time (magenta dashed). Propagation speeds (white-black dashed) correspond to the range of *Washburn et al.* [2011] observations (0.04–0.46 m/s) and the approximate modeled plume propagation (0.20 m/s).

A scaling for the transport by such plumes can be similarly derived,

$$Q \propto \frac{c_w A_p}{(1+c_w/c_\alpha)}, \tag{6}$$

where $A_p = h_p W_p/2$ is the cross-sectional area of the plume (see also equation (7) in *Lentz and Helfrich* [2002]).

5.2. Observed and Modeled Plume Characteristics

5.2.1. Plume Arrival and Characteristics

Buoyant plume arrival at along-coast locations on the SMB inner shelf is identified by the rapid increase in depth-averaged temperature $\overline{T}$ (Figures 10a and 10b). From observations, plume arrival at each mooring $t_a(y)$ is determined from local maxima in the first time derivative of $\overline{T}$ [see *Washburn et al.*, 2011 for details]. The $\overline{T}$ increase propagates northward as it is first observed at ARG, followed by PUR and finally SAL (Figure 10a). The modeled front also propagates

northward, however is not as sharp as observed (Figure 10b). A similar northward-propagating signal can be seen in modeled depth-averaged poleward velocity as the largest poleward flows are associated with the arrival of the temperature increases (not shown). From a time-latitude plot of $\bar{T}^{(m)}$, $t_a(y)^{(m)}$ at modeled moorings roughly coincide with the arrival of the 14.5°C isotherm. The arrival of this isotherm herein determines $t_a(y)^{(m)}$ (Figure 10c). In addition to the poleward-propagating plume, $\bar{T}^{(m)}$ is highly variable including cold water pockets that are advected past the virtual moorings on tidal timescales. The linear regression slope between latitude and time yields an average propagation speed $c_p^{(m)}=0.20\pm0.03$ m s^{-1} of the modeled plume (Figure 10c). This value is well within the range of propagation speeds noted in *Washburn et al*. [2011]. The confidence interval in modeled speed is due to differences in isotherm choice (13–16°C). Confidence intervals of the regression slope are smaller.

The change in water column temperature and stratification associated with the arrival of the plume are determined by

$$\Delta X = \langle X \rangle_+ - \langle X \rangle_- . \tag{7}$$

Here, X is either temperature (T) or vertical thermal stratification ($\partial T/\partial z$) and $\langle . \rangle$ represents a temporal average applied over the 24 h prior to (–) and after (+) plume arrival. For example, an average of the three inner-shelf moorings shows that the plume depth-averaged temperature increased $\Delta\bar{T}^{(o)}=2.4$°C. However, the model average over ARG, PUR, and SAL is smaller $\Delta\bar{T}^{(m)}=1.3$°C, consistent with the less sharp modeled plume.

At the shallow inner-shelf mooring locations, plume arrival increased water temperature throughout the water column. This is not the case in deeper water as evidenced by an across shelf transect of temperature increase $\Delta T^{(m)}$ (Figure 11a). In deeper water, the region of large temperature increase ($\Delta T > 1.3$°C) is confined to the near surface (< 25 m depth). At the outer-shelf SMB mooring (Latitude of 34.80°N), similar temperature increases associated with the plume are present in the observations and model where at depth temperature loggers ($z \leq -45$ m) do not register the increase.

In addition to temperature increases at $z > -25$ m, the plume also alters the thermal stratification across the shelf (Figure 11b). A similar modeled and observed structure to the stratification variations can be seen. In the near-surface, the water column becomes less stratified with plume arrival, indicating a thermal plume that is well-mixed in this region. Below the well-mixed layer, the plume increases stratification across the shelf with a maximum increase in stratification at about 10 m water depth (Figure 11b). The $\Delta T=1.3$°C contour encompasses the majority of the stratification increase and is subsequently considered the bounding region of the plume (Figure 11b).

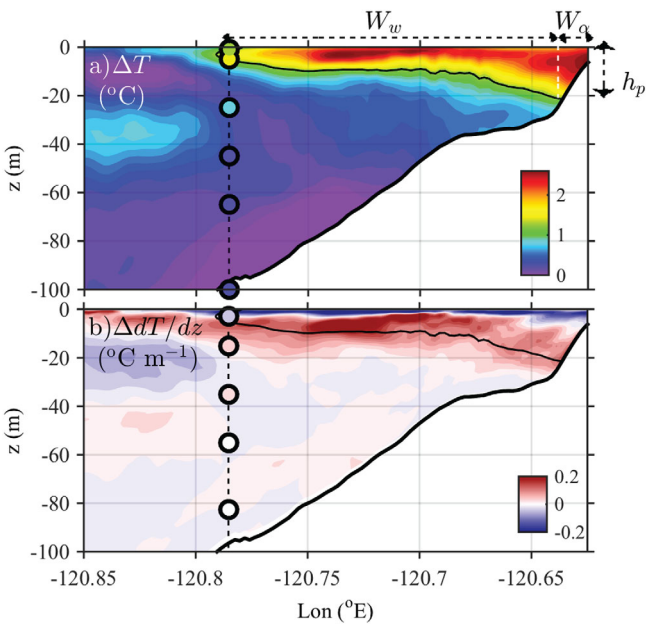

Figure 11. Cross-shelf transect of (a) plume temperature increase (ΔT) and (b) stratification increase ($\Delta dT/dz$) at t_a for the latitude of the SMB mooring (34.80°N). In both plots, modeled results are contoured and observations from the SMB mooring are shown as filled circles at their deployed longitude and depth. The black contour line denotes $\Delta T=1.3$°C, that is overlaid on both plots.

Modeled plume dimensions W_w, W_α, and h_p are extracted from transects of ΔT at each latitude (e.g., Figure 11). At the surface, the offshore distance where plume temperature increase $\Delta T=1.3$°C denotes the total width of the plume W_p. Similarly, the offshore distance where near-bottom $\Delta T=1.3$°C denotes the slope-controlled width of the plume W_α. The water depth at this location is the plume depth h_p. The width of the surface-trapped portion of the plume is determined from (5), $W_w=W_p-W_\alpha$.

5.2.2. Plume-Following Reference Frame

The evolution of plume dimensions and characteristics are placed in a

poleward-propagating reference frame determined by modeled plume arrival on the inner shelf $t_a(y)^{(m)}$. Note that this indicates the along-shore position where the buoyant plume is attached to the coast, not necessarily the along-shore position of the leading edge of the plume nose which is located offshore. In this reference frame, plume dimensions and characteristics (denoted with subscript "p") are extracted from the model results (Figure 12). Similar to the definition of plume temperature increase equation (7), the characteristic plume temperature is determined from a 24 h average after plume arrival ($T_p = \langle T \rangle_+$). The same procedure is applied to determine the surface plume characteristic (denoted with subscript "sp") temperature and poleward velocity ($v_{sp} = \langle v_s \rangle_+$) at each latitude.

In this reference frame, the largest surface plume temperature T_{sp} is found offshore of the 50 m isobath near the plume leading edge (Figure 12a). As the plume propagates poleward, the width of the high T_{sp} region decreases and the near-surface plume temperature T_{sp} also decrease as evidenced by the termination of the 17°C isotherm around SAL. Plume width W_p (marked by magenta dots in Figure 12a) also decreases northward. The offshore extent of the plume initially follows the 16°C isotherm (until ≈ 34.9°N), where the plume region departs from the 16°C isotherm farther north indicating the importance of other sources of thermal variability at these times relative to the plume (Figure 12a).

In contrast to the plume surface temperature decrease, plume bottom temperature (13.5−−14°C) and its cross-shore location (consistently found in water depths 20 m $\leq h_p \leq$ 30 m) remain fairly constant following the plume (not shown). Plume temperature T_p decreases toward the coast (Figures 12c and 12e) in part due to the plume arriving at the coast after it has arrived farther offshore. At 34.95°N, just north of a headland (SAL, upper dashed line in Figure 12a), the temperature decrease from the offshore maxima toward the shore

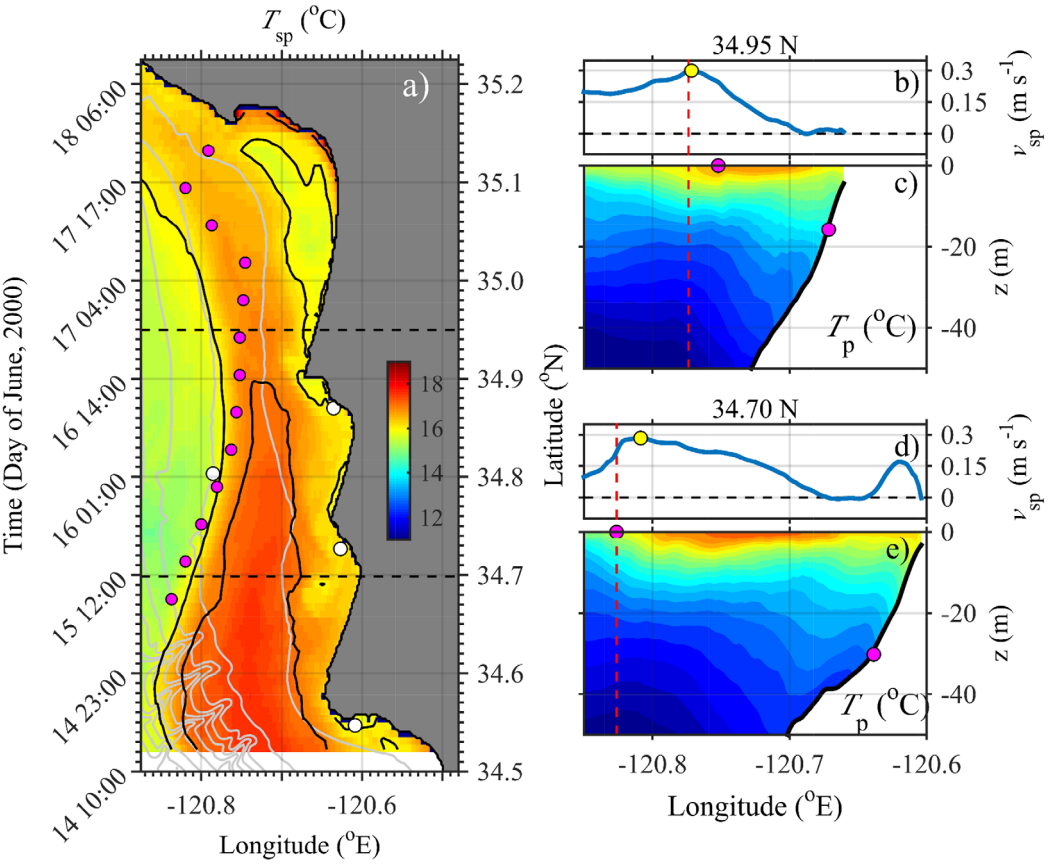

Figure 12. Plume characteristics in plume-following coordinates. (a) Plume surface temperature T_{sp} versus latitude or time, and longitude with the 16 and 17°C isotherms contoured black. Magenta dots delineate plume width as described in section 5.2.2. Isobaths are contoured gray in 50 m increments. (b, d) Transects of plume surface northward velocity v_{sp}, (c, e) transects of plume temperature T_p at the (b, c) northern and (d, e) southern transects denoted by black-dashed lines in Figure 12a. In Figures 12b and 12d, yellow dot denotes maximum v_{sp}. Magenta dots denote the surface and bottom extent of the plume as described in section 5.2.2. Color range used in Figures 12c and 12e is the same as in Figure 12a. Vertical red-dashed line denotes location of maximum surface cross-shore temperature gradient.

Table 2. Comparison of Modeled (m) to Observed (o) Plume Characteristics[a]

	c_p (m s^{-1})	$\Delta\bar{T}$ (°C)	g' ($\times10^{-3}$m^2 s^{-1})	Q (10^5m^3 s^{-1})	c_w (m s^{-1})	c_α (m s^{-1})	c_w/c_α	W_p (km)
(o)	0.04–0.46	2.4	4.8	0.4–2	0.41 (h_p = 40 m)	0.36	1.14	8–16
(m)	0.17–0.23	1.3	2.6	0.7	0.23 (h_p = 20 m)	0.20	1.08	10–23

[a]Comparison of modeled (m) to observed (o) plume features between inner-shelf ARG–SAL moorings. Definition of $g\prime$, calculation of plume speed c_p, and temperature increase $\Delta\bar{T}$ are described in section 5.2. Equations to estimate c_w and c_α are (1) and (3), respectively. W_p is plume width (5).

(≈1°C) is fairly weak (Figure 12c). However, at 34.7°N at the location of the embayment between the ARG and PUR headlands (lower dashed line in Figure 12a), the shoreward temperature decrease is more substantial (≈2°C, Figure 12c) due to colder water retained in headland embayments [e.g., *Gan and Allen*, 2002b].

Near the surface, at the offshore edge of the modeled plume, the cross-shore momentum balance is approximately geostrophic as the maxima in northward velocity coincides with the strongest cross-shore surface temperature gradient (Figures 12b–12e). A plume momentum balance is given in section 6.2.1. At 34.95°N the cross-shore profile of alongshelf velocity (Figure 12b) is consistent with the simple scalings of *Lentz and Helfrich* [2002] (Figure 9). At 34.7°N the alongshelf velocity profile (Figure 12d) also is consistent with simple scalings at >5 km offshore. However, the alongshelf velocity profile onshore within the embayment is more complex with a secondary maximum (Figure 12d), reflecting the role of headland topography.

Observed plume properties of *Washburn et al*. [2011] are compared to modeled plume properties (Table 2). Observed (°) values reported for the change in depth-averaged temperature $\Delta\bar{T}$, and the thermally induced reduced gravity $g'=\alpha g\Delta\bar{T}$, where α is the coefficient of thermal expansion of seawater, are estimated for this specific event. Observed c_α is calculated using (3) with a bottom slope $\theta=7.2\times10^{-3}$, representative of the SMB shelf. The range of observed phase speed c_p is taken from the composite of all reported events and observed plume width is taken from a composite of five HF radar-observed events [*Washburn et al*., 2011]. Volume transport Q and plume depth h_p are not directly observed and instead are estimated from the scaling equations (1–4). Methods to estimate modeled plume properties (m), except for Q are described in section 5.2. Modeled Q is given by the volume integrated northward flow of plume water at the southern boundary of the **L3** domain (at 34.45°N, north of Pt. Conception, Figure 2),

$$Q(t)^{(m)}=\int_{-L}^{0}\int_{-h}^{0} v_* dz dx;\ v_*=\begin{cases} v(x,z,t), & T\geq 14^\circ C \\ 0, & T<14^\circ C \end{cases} \tag{8}$$

where $x=-L$ is the offshore boundary of the **L3** domain. Modeled plume transport is temporally averaged over the event duration (14–18 June). This poleward transport originates as a westward flow of warm water leaving the SBC. An estimate of the volume integrated $T\geq 14$°C westward transport is about 50% higher than $Q^{(m)}$, as not all water leaving the SBC flows poleward.

The propagation speed for the modeled front is similar to observed and to the theoretical phase speed of a buoyant coastal plume with both surface-trapped and slope-controlled dynamics (Table 2). As noted earlier, modeled temperature increases $\Delta\bar{T}^{(m)}$ and $g'^{(m)}$ are less than the observed values, which are also reflected in the reduced phase speed estimates of the surface-trapped c_w and slope-controlled c_α plumes relative to those observed. Modeled plume depth $h_p^{(m)}$ is also shallower than inferred $h_p^{(o)}$. Differences between modeled and inferred plume transports and depth indicate that direct observations are needed. Although individual scaled propagation speed values differ between the observations and the model, the relevant parameter governing plume dynamics, the c_w/c_α ratio is slightly above 1 (Table 2). This is consistent with a buoyant plume that has both surface-trapped and slope-controlled characteristics and suggests that the degree to which buoyant plume dynamics are controlled by one or the other is similar in both the observations and the model.

6. Discussion

6.1. Plume Narrowing

As the modeled plume propagates poleward over the SMB shelf, it undergoes substantial evolution including a decrease in plume reduced gravity g' (Figure 13a) and a decrease in plume width ("narrowing"). These behaviors have also been noted in a many-event composite of plume observations [*Melton et al*., 2009;

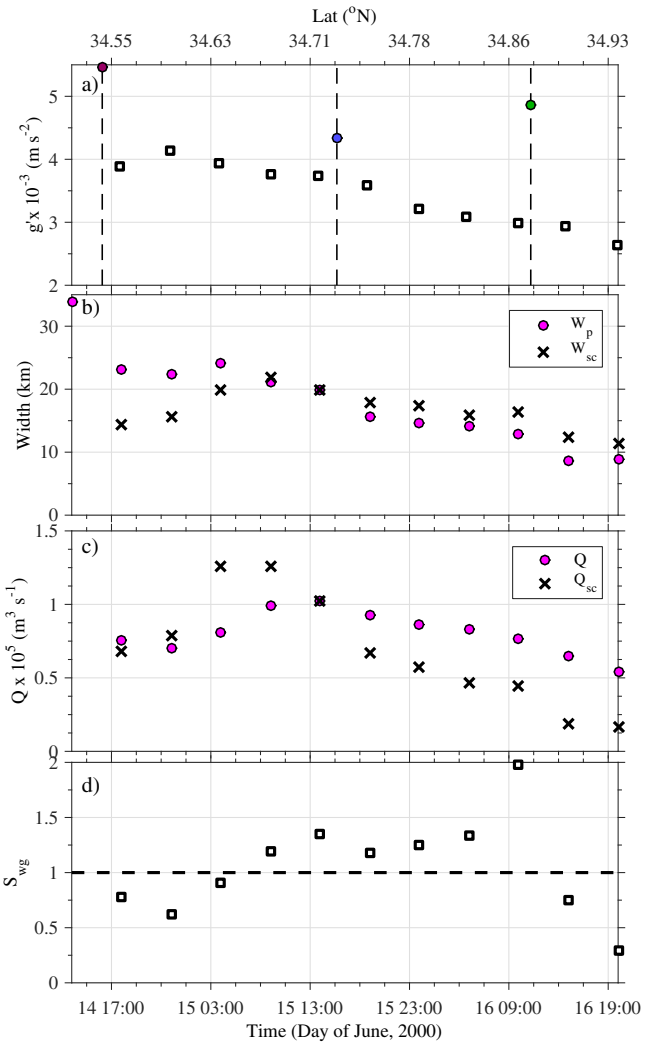

Figure 13. (a) Reduced gravity $g\prime$, (b) modeled plume width $W_p = W_w + W_z$, (c) modeled plume transport Q, (d) nondimensional wind-strength parameter S_{wg} (11) following *Whitney and Garvine* [2005], as functions of latitude or time. In (a), vertical-dashed lines denote the latitudes of inner-shelf moorings ARG, PUR, and SAL, and colored circles denote mooring-observed $g\prime$. In Figure 13b, W_p (magenta dots) are extracted from modeled transects (section 5.2.2), and compared to scaled width W_{sc} (black x) from (5). In Figure 13c, Q (magenta dots) are extracted from modeled output and compared to scaled transport Q_{sc} (black x) from (5).

Washburn et al., 2011]. Two possible mechanisms for plume narrowing are explored for the modeled event; a predicted response due to evolving plume reduced gravity $g\prime$, and the plume response to downwelling-favorable wind forcing [*Lentz and Largier*, 2006; *Moffat and Lentz*, 2012; *Mazzini et al.*, 2014].

From estimates of $c_w^{(m)}$ and $c_\alpha^{(m)}$, the plume width decrease can be predicted by the scaling equation (5). The surface-trapped width $W_w \propto \sqrt{g'h_p}/f$ [*Yankovsky and Chapman*, 1997; *Lentz and Helfrich*, 2002] is a function of both $g\prime$ and h_p, thus a buoyant plume with slowly decreasing $g\prime$ is expected to narrow barring changes in h_p. The applicability of this scaling to the modeled plume is tested by finding a scaled plume width W_{sc},

$$W_{sc} = M_w \left[\frac{c_w^{(m)}}{f} \left(1 + c_w^{(m)} / c_\alpha^{(m)} \right) \right]. \quad (9)$$

where M_w is a constant solved for by linear regression. The regression between $W_p^{(m)}$ and W_{sc} predicts 40% of the along-shelf $W_p^{(m)}$ variance, with a best-fit $M_w = 2.4$ (Figure 13b) consistent with the expected O(1) scaling [*Lentz and Helfrich*, 2002]. Similarly, the scaled modeled plume transport Q_{sc} is tested with,

$$Q_{sc} = M_Q \left[\frac{c_w^{(m)} h_p W_p}{2\left(1 + c_w^{(m)} / c_\alpha^{(m)} \right)} \right]. \quad (10)$$

The regression between $Q^{(m)}$ and Q_{sc} is best-fit with $M_Q = 2.0$ (Figure 13c) also consistent with the expected O(1) scaling. Agreement with these scalings indicates that the quasi steady assumptions of the theory are applicable to the modeled buoyant plume during its poleward propagation.

During the reversal event, downwelling-favorable wind is fairly weak ($\approx 2\,m\,s^{-1}$) but persistent (Figure 3a). *Whitney and Garvine* [2005] developed a wind strength index to assess the relative importance of wind forcing to buoyancy, through a ratio of velocity scales,

$$S_{wg} = \frac{v_{wind}}{v_p}. \quad (11)$$

Here, v_{wind} is an estimate of the surface current driven by the principal axis wind speed V, approximated by equating the quadratic surface and bottom along-shelf stresses $v_{wind} = 2.65 \times 10^{-2} V$ [*Whitney and Garvine*, 2005]. The buoyancy velocity scale is estimated as the time-varying along-shelf velocity associated with the plume v_p. Throughout the period of poleward-flow $S_{wg} \approx 1$, suggesting that the weak downwelling-favorable winds cannot be ruled out as a driver of decreasing plume width (Figure 13d) [e.g., *Lentz and*

Largier, 2006; *Moffat and Lentz*, 2012]. The numerical model also includes other realistic ocean processes which can affect buoyant coastal plumes such as time-varying discharge [*Yankovsky et al*., 2001], ambient background currents [*Fong and Geyer*, 2002], and bathymetric variability [*Pimenta et al*., 2010]. The impact of multiple other processes on the modeled thermal plume is difficult to disentangle with a single realistic realization. To disentangle these processes, sets of idealized numerical experiments are necessary. The relative success of the simple scaling theory [*Lentz and Helfrich*, 2002] in both this modeled thermal plume and with ensembles of plume observations [*Melton et al*., 2009; *Washburn et al*., 2011] suggest that the scaling theory describes the thermal plume dynamics to first order.

6.2. Surface-Trapped and Slope-Controlled Regions

Laboratory studies suggest the importance of bottom stress in the plume along-shelf momentum equation is confined to the onshore, slope-controlled region ($h < h_p$) [e.g., *Lentz and Helfrich*, 2002]. Direct observations of these dynamics in realistic environments are limited as most observations detail surface-trapped plume dynamics [e.g., *Lentz et al*., 2003]. Contrasting onshore and offshore dynamics are illuminated by the model results here.

6.2.1. Momentum Balances

The observed and modeled SBC plume has features consistent with both surface and bottom-slope controlled plumes and thus the momentum balance should be distinct in the surface-trapped ($x < x_p$) and bottom-slope controlled ($x > x_p$) portions of the plume. From model diagnostics, terms in the depth-averaged momentum equation are extracted. For example, the north-south-oriented momentum balance terms are

$$\underbrace{\partial_t \bar{v}}_{\text{ACC}} = \underbrace{-\frac{1}{\rho_0}\partial_y P}_{\text{PRS}} - \underbrace{f\bar{u}}_{\text{COR}} - \underbrace{NLN^y}_{\text{NLN}} - \underbrace{\frac{\tau_b^y}{\rho_0 h}}_{\text{BSR}} + \underbrace{\frac{\tau_s^y}{\rho_0 h}}_{\text{SSR}}. \tag{12}$$

These include the local acceleration (ACC), pressure gradient (PRS), Coriolis acceleration (COR), bottom stress (BSR), and surface stress (SSR). The nonlinear advective term (NLN) is the sum, $\bar{u}\partial_x\bar{v}+\bar{v}\partial_y\bar{v}$. Terms in equation (12), and a similar equation for the east-west-oriented balance, are taken from the latitude of Pt. Purisma (34.73°N) and rotated into the local along and cross-shore directions as determined from the principal axes of the depth-averaged flow. The root-mean-square magnitudes of the different terms are calculated from a 24h period surrounding plume arrival (t_a).

Depth-averaged momentum balances are first examined in 50 m water depth, near the plume core, where isobaths are mostly oriented north-south with little curvature (Figures 14a and 14c). The dominant cross-shore momentum balance is geostrophic, with little contribution from the other terms in the momentum equation (Figure 14a). The along-shore balance has contributions from the nonlinear advective terms and local acceleration, although these are both smaller than the pressure gradient and Coriolis terms, and all terms are a factor of three smaller than those in the cross-shelf balance (Figure 14c). These are consistent with the momentum balance expected for surface-trapped plumes [*Lentz et al*., 2003; *Lentz and Helfrich*, 2002].

At 15 m water depth, where isobaths follow the curved coastline around the capes (Figure 2), although the cross-shore momentum balance is still primarily geostrophic, there are nonnegligible contributions from the nonlinear and local acceleration terms (Figure 14b). In the along-shelf momentum equation, the pressure gradient, nonlinear, and advective acceleration terms are the largest contributors indicating the importance of nonsteady advection (Figure 14d). Root-mean-square of the bottom stress term is about one-third the magnitude of pressure gradient, nonlinear, and advective acceleration, but still important when compared to the other momentum equation terms and consistent with a bottom-slope controlled plume [*Lentz and Helfrich*, 2002].

6.2.2. Shallow-Water Vorticity

A flow characteristic easily calculated from numerical model output, although difficult to observe, is plume vorticity. The barotropic plume vertical vorticity ζ_p,

$$\zeta_p = \partial_x \bar{v}_p - \partial_y \bar{u}_p \tag{13}$$

is calculated from the depth-averaged horizontal velocities associated with plume arrival ($\bar{u}_p, \bar{v}_p$). Onshore of the 50 m isobath, barotropic plume vorticity is ≈ 5 times stronger than the time-averaged vorticity (not shown) at these modeled inner-shelf water depths (Figure 15). Following the plume, the onshore vorticity signal is similar to that of a transient jet with anticyclonic ($\zeta_p < 0$) vorticity on the shoreward side and

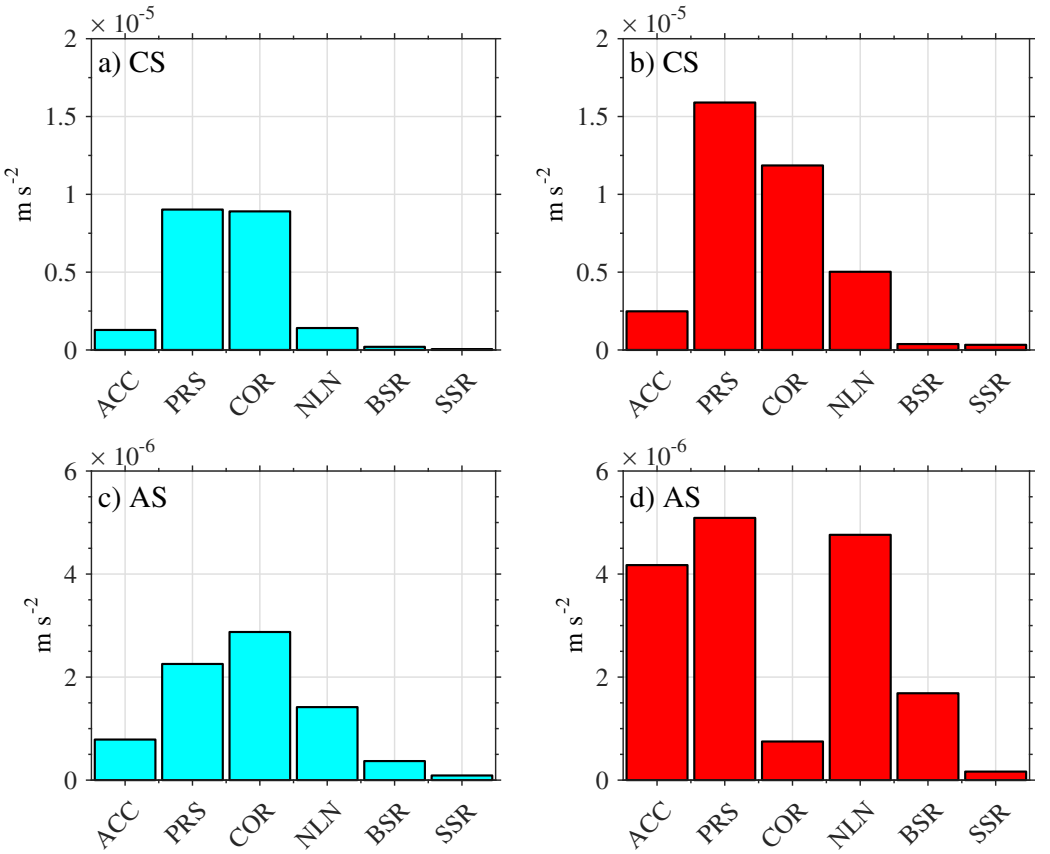

Figure 14. Root mean square (RMS) of depth-averaged (upper) cross-shore and (lower) along-shore momentum balance terms at the PUR latitude (34.73°N). In (a, c) outer-shelf (h = 50 m) terms in cyan. In (b, d) inner-shelf (h = 15 m) terms in red. The RMS momentum balance terms are calculated over a ±12 h period surrounding plume arrival and include the local acceleration (ACC), pressure gradient (PRS), Coriolis acceleration (COR), nonlinear advective (NLN), bottom stress (BSR), and surface stress (SSR).

cyclonic ($\zeta_p < 0$) vorticity seaward (Figure 15). Normalized by the Coriolis frequency and interpreted as a Rossby number, the dimensionless vorticity is $O(1)$, indicating a submesoscale flow feature [e.g., *Capet et al.*, 2008]. The high vorticity flow follows the coastline topography and extends ≈ 5 km from the coast, on the order of the internal Rossby deformation radius ($\sqrt{g'h_p}/f$). Offshore, near the 50 m isobath, a much smaller $O(0.1)$ nondimensional plume vorticity is visible due to horizontal shear in the predominantly geostrophic plume core (Figure 15).

Although vorticity sources widely vary and can include the advection of vorticity and vortex stretching due to flow separation, a portion of this onshore vorticity is a consequence of a region with negligible bottom stress (the surface-trapped plume portion, $x < x_p$) adjacent to a region where bottom stress is important (the slope-controlled portion, $x > x_p$). Where coastal flows encounter spatially variable bottom stress, transient vertical vorticity can be generated by two additional mechanisms: slope torque, which generates vorticity due a greater depth-distributed bottom stress in shallower water, and speed torque due to the quadratic formulation of bottom stress, whereby stronger flows experience stronger bottom stress [e.g., *Signell and Geyer*, 1991]. Over the sloping SMB shelf, the root-mean-squared bottom stress associated with the buoyant plume has significant cross-shore structure ranging from a maximum at about 4×10^{-6} ms^{-2} in 8 m water depth decreasing rapidly to $<0.5\times10^{-6}$ ms^{-2} over a distance of approximately 6 km (not shown). Along with vorticity advection and vortex stretching, both bottom stress mechanisms appear to contribute to generating the onshore vorticity structure.

6.3. The Effect of Excluding Tides

To isolate the effect of tides on the modeled plume, an additional simulation (denoted NT) is downscaled from **L1** to **L3** without tidal boundary forcing. Although the larger-scale temperature and flow features are

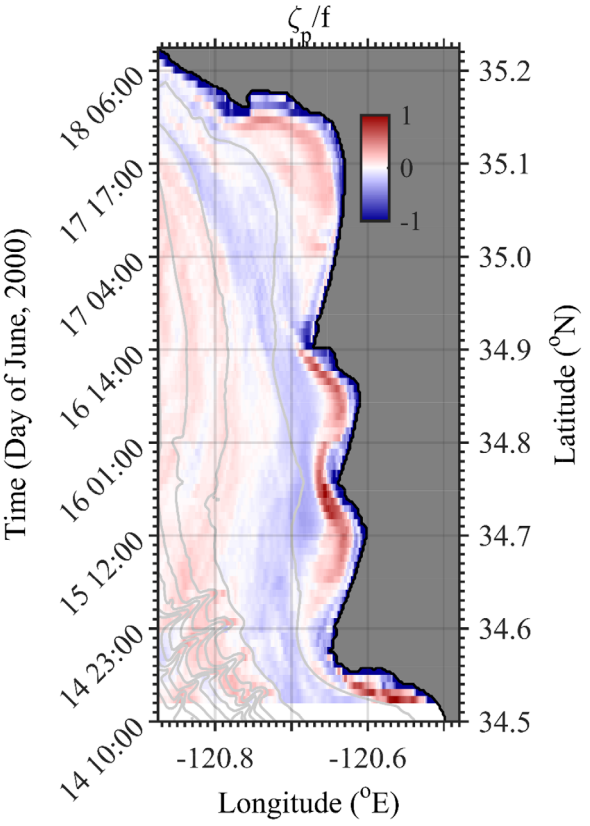

Figure 15. Depth-averaged plume vorticity ζ_p normalized by the Coriolis frequency f as a function of latitude or time and longitude in plume-following coordinates as described in text and Figure 12. Isobaths are contoured gray in 50 m increments.

qualitatively similar in with tide (WT) and without tide (NT) simulations, there are significant differences. The NT simulation is 0.5°C warmer near the surface due to decreased mixing. Model mixing is diagnosed by comparing the time, depth, and cross-shelf (water depth <100 m), averaged vertical eddy diffusivity $\langle K_T \rangle_{t,z,x}$ between the WT and NT cases. The NT $\langle K_T \rangle_{t,z,x} = 10^{-3}\ m^2\ s^{-1}$, about 1.5 times smaller than WT. Idealized two-dimensional (x, z) models have shown that the interaction of tidal and subtidal wind-driven processes increases mixing coefficients in ROMS simulations due to both barotropic [*Castelao et al.*, 2010] and baroclinic tides [*Kurapov et al.*, 2010].

Neglecting tidal forcing also affects some characteristics of the poleward-propagating buoyant plume. NT plume surface temperature is warmer because of less vertical mixing within the **L3** domain, as well as a less mixed water mass incoming from the southern boundary (mixing is also reduced within the **L2** simulation). The persistence of the plume, as diagnosed by the rate of reduction in plume-induced depth-averaged temperature increase $\Delta\bar{T}$ as it propagates northward, also differs between the two simulations. With tides, the rate of decrease in $\Delta\bar{T}$ was about 0.5°C per day, almost twice the reduction in $\Delta\bar{T}$ for the NT simulation. This indicates that without tides, a simulated thermal plume potentially propagates farther poleward along the coast and/or persists on the shelf for longer duration.

7. Summary

A nested realistic Regional Ocean Model (ROMS) is configured to simulate the coastal ocean response to wind relaxation around Pt. Conception, CA. The model reproduces reasonably well the statistics of observed in situ subtidal water column temperature and velocity at both outer and inner-shelf mooring locations. The model also reproduces kinematic properties including the ≈ 5°C temperature change, stratification variation, and flow structures associated with a poleward-propagating buoyant warm plume originating from the Santa Barbara Channel. The modeled plume provides a first approximation of how difficult-to-observe features, such as cross-shore-depth sections (x, z), momentum balances, and vorticity can be manifested.

The modeled plume agrees with a theoretical scaling for intermediate buoyant plumes [*Lentz and Helfrich*, 2002], with distinct onshore and offshore dynamics. In the offshore (>30 m depth) region, where the plume velocities are strongest and controlled by surface-trapped dynamics, the depth-averaged cross-shore momentum balance is geostrophic and bottom stress is unimportant. Within 5 km from shore, onshore of the 30 m isobath, the plume water mass extends to the bottom. Here, the dynamics are consistent with slope-controlled plumes and bottom stress is important in the alongshore momentum equation contributing to the generation of vertical vorticity. This vorticity is an order of magnitude larger than the vorticity due to horizontal shear in the geostrophic plume core.

Additional simulations without tidal forcing show that modeled surface temperatures are biased 0.5°C higher when excluding tidal mixing processes. This has important implications for the along-shore propagation distance and persistence of the modeled plume on the SMB shelf.

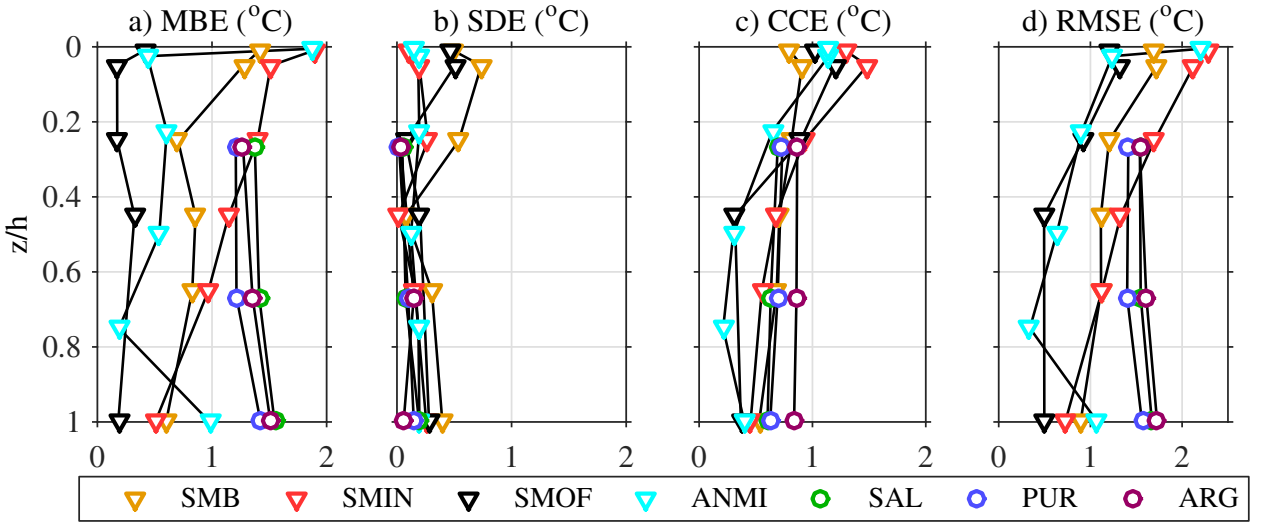

Figure A1. Evaluation of subtidal-frequency model-data differences as in (equation (A1)). Values are reported as the square of each term (units are in °C). From left to right, plots are (a) mean bias error (MBE), (b) standard deviation error (SDE), (c) model-data cross correlation error (CCE), and (d) root mean square error (RMSE). Triangles (circles) denote outer (inner) shelf mooring locations.

Appendix A: Model-Data Differences

Model-data differences in subtidal temperature are quantified by root-mean-squared error, partitioned into separate components [e.g., *Oke et al.*, 2002; *Wilkin*, 2006; *Liu et al.*, 2009]. The root-mean-squared error is $\mathrm{RMSE}=\langle(m_i-o_i)^2\rangle^{1/2}$ where m_i and o_i are the i-th modeled and observed subtidal temperature $T(t)$ and angle brackets denote a time-mean. RMSE is written as the sum of three terms such that:

$$\mathrm{RMSE}=\left[\underbrace{(\langle m\rangle-\langle o\rangle)^2}_{\mathrm{MBE}^2}+\underbrace{(S_m-S_o)^2}_{\mathrm{SDE}^2}+\underbrace{2S_mS_o(1-\mathrm{CC})}_{\mathrm{CCE}^2}\right]^{1/2}. \tag{A1}$$

(A1) Terms in (A1) are (1) a mean bias error, MBE, (2) standard deviation error, SDE, where S_m and S_o are the respective model and observed subtidal standard deviations, and (3) the cross-correlation error CCE, proportional to the correlation between observed and modeled temperature.

Model temperature error terms are largest within the upper 20 m of the water column. Normalized by water depth, profiles of RMSE reach $\approx 2^{\circ}$C in the near surface at outer-shelf moorings and appear depth-uniform at shallow inner-shelf moorings. At all moorings except SMOF and the ANMI middle water column temperature loggers, MBE is the largest source of model-data misfit (Figure A1). Taking an average of all temperature errors, CCE is about 40% of MBE and SDE is the smallest term (20% of MBE). Small SDE indicate that subtidal temperature variability is well reproduced by nested models which resolve processes across the outer and inner continental shelf [*Kumar et al.*, 2015]. With improved surface flux and lateral boundary conditions (perhaps through data assimilation), MBE is potentially reduced.

Acknowledgments
We gratefully acknowledge support from the Office of Naval Research through award N00014-14-1-0556 to Georgia Institute of Technology and N00014-14-1-0553 to Scripps Institution of Oceanography. S.H.S. acknowledges National Science Foundation support through OCE-1521653. Santa Barbara Channel-Santa Maria Basin Coastal Circulation Study data were provided by Clint Winant and Myrl Hendershott, supported by the Minerals Management Service. In accordance with AGU policy, data are accessible through SIO Information Technology, for details email ssuanda@ucsd.edu. Partnership for Interdisciplinary Studies of Coastal Oceans (PISCO) moorings are funded primarily by the Gordon and Betty Moore Foundation and David and Lucile Packard Foundation as well as NSF awards OCE-0957948 to UCSB and UConn and OCE-9982105, OCE-0620276, OCE-1232779, OCE-1031893, OCE-1220359, OCE-1041229, and OCE-0352187 to UCSB; M.F. acknowledges NASA awards NNX10AO94G to UCSB and NNX14AI06G to UConn. These data are available at http://www.piscoweb.org/. We thank Maria Aristizabal and Chris Gotschalk for assistance with data processing and Sarah Giddings for useful discussions on the manuscript.

References

Aristizábal, M. F., M. R. Fewings, and L. Washburn (2016), Contrasting spatial patterns in the diurnal and semidiurnal temperature variability in the Santa Barbara Channel, California, *J. Geophys. Res. Oceans*, *121*, 427–440, doi:10.1002/2015JC011239.

Auad, G., M. C. Hendershott, and C. D. Winant (1999), Mass and heat balances in the Santa Barbara Channel: Estimation, description and forcing, *Prog. Oceanogr.*, *43*(1), 111–155, doi:10.1016/S0079-6611(99)00006-3.

Brink, K. H., and R. D. Muench (1986), Circulation in the Point Conception-Santa Barbara Channel region, *J. Geophys. Res.*, *91*(C1), 877–895, doi:10.1029/JC091iC01p00877.

Buijsman, M. C., Y. Uchiyama, J. C. McWilliams, and C. R. Hill-Lindsay (2012), Modeling semidiurnal internal tide variability in the Southern California Bight, *J. Phys. Oceanogr.*, *42*(1), 62–77, doi:10.1175/2011JPO4597.1.

Capet, X., J. C. McWilliams, M. J. Molemaker, and A. F. Shchepetkin (2008), Mesoscale to submesoscale transition in the California Current System. Part I: Flow structure, eddy flux, and observational tests, *J. Phys. Oceanogr.*, *38*(1), 29–43, doi:10.1175/2007JPO3671.1.

Castelao, R., R. Chant, S. Glenn, and O. Schofield (2010), The effects of tides and oscillatory winds on the subtidal inner-shelf cross-shelf circulation, *J. Phys. Oceanogr.*, *40*(4), 775–788, doi:10.1175/2009JPO4273.1.

Chapman, D. C. (1985), Numerical treatment of cross-shelf open boundaries in a Barotropic Coastal Ocean Model, *J. Phys. Oceanogr.*, *15*(8), 1060–1075, doi:10.1175/1520-0485(1985).
Connolly, T. P., B. M. Hickey, I. Shulman, and R. E. Thomson (2014), Coastal trapped waves, alongshore pressure gradients, and the California Undercurrent, *J. Phys. Oceanogr.*, *44*(1), 319–342, doi:10.1175/JPO-D-13-095.1.
Cudaback, C. N., L. Washburn, and E. Dever (2005), Subtidal inner-shelf circulation near Point Conception, California, *J. Geophys. Res.*, *110*, C10007, doi:10.1029/2004JC002608.
Dever, E. P. (2004), Objective maps of near-surface flow states near Point Conception, California, *J. Phys. Oceanogr.*, *34*(2), 444–461, doi: 10.1175/1520-0485(2004).
Dong, C., and L.-Y. Oey (2005), Sensitivity of coastal currents near Point Conception to forcing by three different winds: ECMWF, COAMPS, and blended SSM/I-ECMWF-Buoy winds, *J. Phys. Oceanogr.*, *35*(7), 1229–1244, doi:10.1175/JPO2751.1.
Dong, C., E. Y. Idica, and J. C. McWilliams (2009), Circulation and multiple-scale variability in the Southern California Bight, *Prog. Oceanogr.*, *82*(3), 168–190, doi:10.1016/j.pocean.2009.07.005.
Dorman, C. E., and C. D. Winant (2000), The structure and variability of the marine atmosphere around the Santa Barbara channel, *Mon. Weather Rev.*, *128*(2), 261–282, doi:10.1175/1520-0493(2000)128<0261:TSAVOT>2.0.CO;2.
Doyle, J. D., Q. Jiang, Y. Chao, and J. Farrara (2009), High-resolution atmospheric modeling over the Monterey Bay during AOSN II, *Deep Sea Res., Part II*, *56*, 87–99.
Fewings, M. R., L. Washburn, and J. Carter Ohlmann (2015), Coastal water circulation patterns around the northern Channel Islands and Point Conception, California, *Prog. Oceanogr.*, *138*, 283–304, doi:10.1016/j.pocean.2015.10.001.
Flather, R. (1976), A tidal model of the northwest European continental shelf, *Mem. Soc. R. Sci. Liege*, *10*(6), 141–164.
Fong, D. A., and W. R. Geyer (2002), The alongshore transport of freshwater in a surface-trapped river plume*, *J. Phys. Oceanogr.*, *32*(3), 957–972, doi:10.1175/1520-0485(2002)032<0957:TATOFI>2.0.CO;2.
Gan, J., and J. S. Allen (2002a), A modeling study of shelf circulation off northern California in the region of the Coastal Ocean Dynamics Experiment: Response to relaxation of upwelling winds, *J. Geophys. Res.*, *107*(C9), 3123, doi:10.1029/2000JC000768.
Gan, J., and J. S. Allen (2002b), A modeling study of shelf circulation off northern California in the region of the Coastal Ocean Dynamics Experiment 2. Simulations and comparisons with observations, *J. Geophys. Res.*, *107*(C11), 3184, doi:10.1029/2000JC001190.
Ganju, N. K., S. J. Lentz, A. R. Kirincich, and J. T. Farrar (2011), Complex mean circulation over the inner shelf south of Martha's Vineyard revealed by observations and a high-resolution model, *J. Geophys. Res.*, *116*, C10036, doi:10.1029/2011JC007035.
Haidvogel, D. B., et al. (2008), Ocean forecasting in terrain-following coordinates: Formulation and skill assessment of the Regional Ocean Modeling System, *J. Comput. Phys.*, *227*(7), 3595–3624, doi:10.1016/j.jcp.2007.06.016.
Harms, S., and C. D. Winant (1998), Characteristic patterns of the circulation in the Santa Barbara Channel, *J. Geophys. Res.*, *103*(C2), 3041–3065, doi:10.1029/97JC02393.
Hendershott, M. C., and C. D. Winant (1996), Surface circulation in the Santa Barbara channel, *Oceanography*, *9*(2), 114–121.
Hickey, B. M., E. L. Dobbins, and S. E. Allen (2003), Local and remote forcing of currents and temperature in the central Southern California Bight, *J. Geophys. Res.*, *108*(C3), 3081, doi:10.1029/2000JC000313.
Hodur, R., X. Hong, J. Doyle, J. Pullen, J. Cummings, P. Martin, and M. A. Rennick (2002), The Coupled Ocean/Atmosphere Mesoscale Prediction System (COAMPS), *Oceanography*, *15*(1), 88–98, doi:10.5670/oceanog.2002.39.
Hsu, H.-m., L.-Y. Oey, W. Johnson, C. Dorman, and R. Hodur (2007), Model wind over the Central and Southern California coastal ocean, *Mon. Weather Rev.*, *135*(5), 1931–1944, doi:10.1175/MWR3389.1.
Johansson, M. L., et al. (2015), Seascape drivers of Macrocystis pyrifera population genetic structure in the northeast Pacific, *Mol. Ecol.*, *24*(19), 4866–4885, doi:10.1111/mec.13371.
Kumar, N., F. Feddersen, Y. Uchiyama, J. McWilliams, and W. O'Reilly (2015), Midshelf to surfzone coupled ROMS-SWAN model data comparison of waves, currents, and temperature: Diagnosis of subtidal forcings and response, *J. Phys. Oceanogr.*, *45*(6), 1464–1490, doi:10.1175/JPO-D-14-0151.1.
Kumar, N., F. Feddersen, S. Suanda, Y. Uchiyama, and J. McWilliams (2016), Mid- to inner-shelf coupled ROMS-SWAN model-data comparison of currents and temperature: Diurnal and semidiurnal variability, *J. Phys. Oceanogr.*, *46*(3), 841–862, doi:10.1175/JPO-D-15-0103.1.
Kurapov, A. L., J. S. Allen, and G. D. Egbert (2010), Combined effects of wind-driven upwelling and internal tide on the continental shelf, *J. Phys. Oceanogr.*, *40*(4), 737–756, doi:10.1175/2009JPO4183.1.
Lentz, S. J., and K. R. Helfrich (2002), Buoyant gravity currents along a sloping bottom in a rotating fluid, *J. Fluid Mech.*, *464*, 251–278, doi: 10.1017/S0022112002008868.
Lentz, S. J., and J. Largier (2006), The influence of wind forcing on the Chesapeake Bay buoyant coastal current, *J. Phys. Oceanogr.*, *36*, 1305–1316.
Lentz, S. J., S. Elgar, and R. T. Guza (2003), Observations of the flow field near the nose of a buoyant coastal current, *J. Phys. Oceanogr.*, *33*(4), 933–943, doi:10.1175/1520-0485(2003).
Liu, Y., P. MacCready, B. M. Hickey, E. P. Dever, P. M. Kosro, and N. S. Banas (2009), Evaluation of a coastal ocean circulation model for the Columbia River plume in summer 2004, *J. Geophys. Res.*, *114*, C00B04, doi:10.1029/2008JC004929.
Marchesiello, P., J. C. McWilliams, and A. Shchepetkin (2001), Open boundary conditions for long-term integration of regional oceanic models, *Ocean Modell.*, *3*(1), 1–20.
Mark, D. J., E. A. Spargo, J. J. Westerink, and R. A. Luettich (2004), ENPAC 2003: A Tidal constituent database for eastern North Pacific Ocean, *Tech. Rep. ERDC/CHL-TR-04-12*, Coastal and Hydraul. Lab., U.S. Army Corps of Eng., Washington, D. C.
Mason, E., J. Molemaker, A. F. Shchepetkin, F. Colas, J. C. McWilliams, and P. Sangr (2010), Procedures for offline grid nesting in regional ocean models, *Ocean Modell.*, *35*(1), 1–15, doi:10.1016/j.ocemod.2010.05.007.
Mazzini, P. L. F., J. A. Barth, R. K. Shearman, and A. Erofeev (2014), Buoyancy-driven coastal currents off Oregon during Fall and Winter, *J. Phys. Oceanogr.*, *44*(11), 2854–2876, doi:10.1175/JPO-D-14-0012.1.
McCreary, J. P. (1981), A linear stratified ocean model of the coastal undercurrent, *Philos. Trans. R. Soc. London A*, *302*(1469), 385–413, doi: 10.1098/rsta.1981.0176.
Melton, C., L. Washburn, and C. Gotschalk (2009), Wind relaxations and poleward flow events in a coastal upwelling system on the central California coast, *J. Geophys. Res.*, *114*, C11016, doi:10.1029/2009JC005397.
Moffat, C., and S. Lentz (2012), On the response of a buoyant plume to downwelling-favorable wind stress, *J. Phys. Oceanogr.*, *42*(7), 1083–1098, doi:10.1175/JPO-D-11-015.1.
Oey, L.-Y., C. Winant, E. Dever, W. R. Johnson, and D.-P. Wang (2004), A model of the near-surface circulation of the Santa Barbara Channel: Comparison with observations and dynamical interpretations, *J. Phys. Oceanogr.*, *34*(1), 23–43, doi:10.1175/1520-0485(2004)034<0023:AMOTNC>2.0.CO;2.

Oke, P. R., J. S. Allen, R. N. Miller, G. D. Egbert, J. A. Austin, J. A. Barth, T. J. Boyd, P. M. Kosro, and M. D. Levine (2002), A modeling study of the three-dimensional continental shelf circulation off Oregon. Part I: Model-data comparisons, *J. Phys. Oceanogr.*, *32*(5), 1360–1382, doi:10.1175/1520-0485(2002)032<1360:AMSOTT>2.0.CO;2.

Pawlowicz, R., B. Beardsley, and S. Lentz (2002), Classical tidal harmonic analysis including error estimates in MATLAB using T_TIDE, *Comput. Geosci.*, *28*(8), 929–937, doi:10.1016/S0098-3004(02)00013-4.

Penven, P., L. Debreu, P. Marchesiello, and J. C. McWilliams (2006), Evaluation and application of the ROMS 1-way embedding procedure to the central California upwelling system, *Ocean Modell.*, *12(12)*, 157–187, doi:10.1016/j.ocemod.2005.05.002.

Pimenta, F. M., A. D. Kirwan, and P. Huq (2010), On the transport of buoyant coastal plumes, *J. Phys. Oceanogr.*, *41*(3), 620–640, doi:10.1175/2010JPO4473.1.

Pringle, J. M., and E. P. Dever (2009), Dynamics of wind-driven upwelling and relaxation between Monterey Bay and Point Arena: Local-, regional-, and gyre-scale controls, *J. Geophys. Res.*, *114*, C07003, doi:10.1029/2008JC005016.

Romero, L., Y. Uchiyama, J. C. Ohlmann, J. C. McWilliams, and D. A. Siegel (2013), Simulations of nearshore particle-pair dispersion in Southern California, *J. Phys. Oceanogr.*, *43*(9), 1862–1879, doi:10.1175/JPO-D-13-011.1.

Shchepetkin, A. F., and J. C. McWilliams (2005), The regional oceanic modeling system (ROMS): A split-explicit, free-surface, topography-following-coordinate oceanic model, *Ocean Modell.*, *9*(4), 347–404, doi:10.1016/j.ocemod.2004.08.002.

Shchepetkin, A. F., and J. C. McWilliams (2009), Correction and commentary for Ocean forecasting in terrain-following coordinates: Formulation and skill assessment of the regional ocean modeling system by *Haidvogel et al., J. Comput. Phys., 227, 3595–3624, J. Comput. Phys.*, *228*(24), 8985–9000, doi:10.1016/j.jcp.2009.09.002.

Signell, R. P., and W. R. Geyer (1991), Transient eddy formation around headlands, *J. Geophys. Res.*, *96*(C2), 2561–2575, doi:10.1029/90JC02029.

Springer, S. R., R. M. Samelson, J. S. Allen, G. D. Egbert, A. L. Kurapov, R. N. Miller, and J. C. Kindle (2009), A nested grid model of the Oregon Coastal Transition Zone: Simulations and comparisons with observations during the 2001 upwelling season, *J. Geophys. Res.*, *114*, C02010, doi:10.1029/2008JC004863.

Veneziani, M., C. A. Edwards, J. D. Doyle, and D. Foley (2009), A central California coastal ocean modeling study: 1. Forward model and the influence of realistic versus climatological forcing, *J. Geophys. Res.*, *114*, C04015, doi:10.1029/2008JC004774.

Wang, D.-P. (1997), Effects of small-scale wind on coastal upwelling with application to Point Conception, *J. Geophys. Res.*, *102*(C7), 15,555–15,566, doi:10.1029/97JC00635.

Warner, J. C., C. R. Sherwood, H. G. Arango, and R. P. Signell (2005), Performance of four turbulence closure models implemented using a generic length scale method, *Ocean Modell.*, *8*(1), 81–113, doi:16/j.ocemod.2003.12.003.

Warner, J. C., B. Armstrong, R. He, and J. B. Zambon (2010), Development of a Coupled Ocean–Atmosphere–Wave–Sediment Transport (COAWST) modeling system, *Ocean Modell.*, *35*(3), 230–244, doi:10.1016/j.ocemod.2010.07.010.

Washburn, L., M. R. Fewings, C. Melton, and C. Gotschalk (2011), The propagating response of coastal circulation due to wind relaxations along the central California coast, *J. Geophys. Res.*, *116*, C12028, doi:10.1029/2011JC007502.

Whitney, M. M., and R. W. Garvine (2005), Wind influence on a coastal buoyant outflow, *J. Geophys. Res.*, *110*, C03014, doi:10.1029/2003JC002261.

Wilkin, J. L. (2006), The summertime heat budget and circulation of southeast New England Shelf Waters, *J. Phys. Oceanogr.*, *36*(11), 1997–2011, doi:10.1175/JPO2968.1.

Winant, C. D., E. P. Dever, and M. C. Hendershott (2003), Characteristic patterns of shelf circulation at the boundary between central and southern California, *J. Geophys. Res.*, *108*(C2), 3021, doi:10.1029/2001JC001302.

Woodson, C. B., L. Washburn, J. A. Barth, D. J. Hoover, A. R. Kirincich, M. A. McManus, J. P. Ryan, and J. Tyburczy (2009), Northern Monterey Bay upwelling shadow front: Observations of a coastally and surface-trapped buoyant plume, *J. Geophys. Res.*, *114*, C12013, doi:10.1029/2009JC005623.

Yankovsky, A. E., and D. C. Chapman (1997), A simple theory for the fate of buoyant coastal discharges, *J. Phys. Oceanogr.*, *27*(7), 1386–1401, doi:10.1175/1520-0485(1997)027<1386:ASTFTF>2.0.CO;2.

Yankovsky, A. E., B. M. Hickey, and A. K. Mnchow (2001), Impact of variable inflow on the dynamics of a coastal buoyant plume, *J. Geophys. Res.*, *106*(C9), 19,809–19,824, doi:10.1029/2001JC000792.